A single multi-scale and multi-sourced semi-automated lineament detection technique for detailed structural mapping with applications to geothermal energy exploration

Abbreviated title: *Multi-scale semi-automated lineament detection*

Christopher M. Yeomans[1*], Hester Claridge[2], Alexander J.L. Hudson[1,2], Robin K. Shail[1], Cees Willems[3], Matthew Eyre[1], Chris Harker[2]

[1]Camborne School of Mines, College of Mathematics, Engineering and Physical Sciences, University of Exeter, Penryn Campus, Penryn, Cornwall, TR10 9FE

[2]Cornish Lithium Ltd, Tremough Innovation Centre, Penryn Campus, Penryn, Cornwall, TR10 9TA

[3]Institute for GeoEnergy Engineering, Energy Academy, Heriot-Watt University, Edinburgh Campus, Currie, EH14 4AP

* correspondence (c.m.yeomans@exeter.ac.uk)

ORCID

CMY: 0000-0002-0364-451X, RKS: 0000-0001-7200-5124, CW: 0000-0002-4502-8598, ME: 0000-00025506674X

Abstract

A multitude of semi-automated algorithms, many incorporating multi-sourced datasets into a single analysis, now exist. However, these operate at a fixed pixel resolution resulting in multi-sourced methods being limited by the largest input pixel size. Multi-scale lineament detection circumvents this issue and allows increased levels of detail to be captured. In this study we present a semi-automated method using bottom-up Object-Based Image Analysis approach to map regional lineaments to a high level of detail. The method is applied to onshore LiDAR data and offshore bathymetry around the Land's End Granite (Cornwall, UK). The method uses three different pixel resolutions to extract detailed lineaments across a 700 km^2 area. The granite displays large-scale NW-SE structures that are considered to be an analogue to fault-hosted geothermal systems in southwest England. Investigation of the lineaments derived from this study show along-strike variations from NW-SE orientations within granite to NNW-SSE within mudstone and reflect structural inheritance of early Variscan structures within Devonian mudstones. This is furthered by analysing these major structures for reservoir potential. Lineaments proximal to these broadly NW-SE features indicate a damage zone approximately 100 m wide is present. These observations provide a preliminary understanding of reservoir characteristics for fault-hosted geothermal systems.

Introduction

Semi-automated lineament detection methods provide a rapid and robust means of mapping structural features at a multitude of scales. A geological lineament, defined as a mappable recti-linear or curvi-linear feature of a surface and distinct from adjacent patterns (O'Leary, 1976), can be mapped to infer faults or fractures within the subsurface. The increasing resolution of remotely sensed data allows more detailed lineament studies over larger areas, making a completely manual analysis out-of-scope for most applications. Therefore, semi-automated methods are now the go-to tool for many practitioners.

There are a variety of published methods for semi-automated lineament detection available on a range of platforms, including tools within mainstream software packages such as PCI Geomatica and Seequent Oasis Montaj or bespoke algorithms (e.g. Rahnama and Gloaguen, 2014a,b; Middleton et al., 2015; Šilhavy et al., 2016; Masoud and Koike, 2017; Yeomans et al., 2019). Many of these are able to analyse multi-source data inputs, however, as yet no algorithm has attempted to combine multi-source and multi-scale input data.

Herein, we use an adaptation of the semi-automated bottom-up Object-Based Image Analysis (OBIA) method of Yeomans et al. (2019). We combine multi-source data from an onshore LiDAR elevation model and offshore bathymetry at three different pixel resolutions to evaluate lineament characteristics over an area of 700 km^2. This is complemented by two localised manual studies which validate the semi-automated method and demonstrate the level of structural detail. The study area is the Land’s End peninsula and adjacent offshore areas in southwest England; the bedrock geology comprises the Land’s End Granite and its Devonian host rocks. It has been selected due to its importance for understanding NW-SE fault zones that are currently being targeted farther east in Cornwall (United Downs Deep Geothermal Power Project near Redruth and the Eden Geothermal Project, St Austell) as fault-hosted deep geothermal reservoirs. The Land's End area is an ideal locality to study these NW-SE fault systems due to the accessibility of granite coastal exposures and the quality of bathymetric data. Exposed bedrock in offshore areas reveals a detailed fault network and these areas can be mapped in detail to give a representative model of the underlying fault network that may be otherwise be obscured in onshore areas.

Lineament networks across the region are investigated with a view to mapping the NW-SE target structures but also to understand other orientations such as NNW-SSE and NNE-SSW features highlighted by Nixon et al. (2012) and ENE-WSW fault-controlled vein (lode) systems further east (Alexander and Shail 1995,1996; Shail and Alexander, 1997). These structures and their interactions with NW-SE systems are investigated based on their host rock and their distance from manually digitised fault traces to determine the presence of damage zones and infer preliminary geothermal reservoir characteristics. This study provides a platform for further modelling of geothermal reservoirs and to provide exploration tool to identify new target structures.

Geological setting

The Upper Palaeozoic geology of southwest England (Figure 1a) comprises low-grade regionally metamorphosed Devonian-Carboniferous sedimentary successions, with minor mafic igneous rocks, that were deformed during the Variscan Orogeny (Carboniferous), which are later intruded by the Cornubian Granite Batholith in the Early Permian (Leveridge and Hartley, 2006; Scrivener, 2006). Three regional deformation events (D1-D3) are recoginised. D1 and D2 structures developed in a NNW-directed thrust-fold belt during Variscan continental collision following the closure of the Rheic-Rhenohercynian Ocean. D3 structures formed during latest Carboniferous to Early Permian post-Variscan regional extension during which thrust faults were reactivated as top-to-the-SSE extensional faults and new higher-angle ENE-WSW striking extensional faults formed (Alexander and Shail, 1995, 1995; Shail and Alexander, 1997; Shail and Leveridge, 2009; Alexander et al., 2019).

INSERT FIGURE 1 (regional geology)

Early Permian magmatism was, in part, synchronous with regional D3 extension and is largely represented by the Cornubian Batholith that was emplaced between 293-275 Ma (Chen et al., 1993, Chesley et al., 1993; Scrivener, 2006; Simons et al., 2016). The Land’s End Granite study area is located approximately mid-way along the batholith, which continues eastwards some 100 km across the SW England peninsula and offshore for a similar distance westwards across the Cornubian Ridge (Evans, 1990). A magmatic-hydrothermal tungsten-tin-copper-zinc orefield was developed contemporaneously with batholith construction and was overwhelmingly fault- and joint -controlled (Chen et al., 1993, Chesley et al., 1993). Extensional fault-controlled vein systems (lodes) are typically ENE-WSW to E-W oriented, reflecting NNW-SSE to N-S extension, and formed synchronously with steeply-dipping NNW-SSE strike-slip transfer faults. The latter stages of mineralisation, presumed associated with the youngest magmatic episodes, are commonly oriented NW-SE to N-S and may reflect a change in regional stress (Shail and Alexander, 1997). The development of Early Permian ENE-WNW to E-W oriented extensional fault systems in the granites and their host rocks was contemporaneous with the formation of extensional sedimentary basins that host Permian 'red bed' successions (Evan, 1990; Alexander et al., 2019).

The subsequent structural evolution of fault networks during the Mid-Permian to Mid-Triassic is poorly constrained but two minor episodes of intraplate shortening (Shail and Alexander, 1997). Regional ENE-WNW extension during the Triassic brought about the extensional reactivation of Early Permian NNW-SSE transfer faults and development of new faults (Shail and Alexander, 1997). It was accompanied by Triassic 'red-bed' sedimentary basin development and a regional Mid-Triassic episode of basinal brine migration through the NW-SE to NNE-SSW extensional fault systems. The resultant basement-hosted 'cross-course' veins offset earlier Permian magmatic-hydrothermal lodes (Scrivener et al., 1994; Gleeson et al., 2000, 2001).

Following the Triassic cross-course event, there is little constraint on the onshore structural evolution until the Cenozoic. An Oligocene intraplate strike-slip tectonic regime resulted in both dextral and sinistral reactivation of NW-SE faults, with displacements of up to several kilometres, along the Sticklepath-Lustleigh Fault Zone in the east of the region (Holloway and Chadwick, 1986).

The Land's End Granite and surrounding area

The Land's End Granite is the youngest of the granite plutons at c. 274-279 Ma (Chen et al., 1993; Chesley et al., 1993) having been intruded into the Upper Devonian Mylor Slate Formation of the Gramscatho Group (Figure 2). It forms the most westerly mainland exposure of the Cornubian Batholith and provides consistent exposure of the granite and its margins in coastal outcrop. The pluton is unusual in shape compared to the other plutons in southwest England, and is characterised by a distinct geomorphology controlled by regularly spaced NW-SE oriented valleys. These features extend offshore, and are observable in the seafloor, where the bedrock is also Mylor Slate Formation. The submerged outcrop provides a highly detailed surface upon which to study fracture networks and trace these back to onshore areas where outcrop is more limited. Offshore areas are susceptible to sediment cover, which obscures the desired bedrock exposure, and the occurrence of sand waves upon these sediments can cause false positive results in lineament studies. However, these are not extensive in the area selected and have been mitigated during post-processing.

INSERT FIGURE 2 (local geological)

Lineament detection methods

As datasets increase in coverage and resolution, semi-automated lineament detection becomes a more efficient choice to the practitioner. Built-in tools to mainstream software are commonly applied but there is an increasing prevalence of bespoke algorithms designed for use within different programming languages such as MATLAB (Rahnama and Gloaguen, 2014a,b), Python (Šilhavy et al., 2016; Karimi and Karimi, 2017) and eCognition's Cognitive Network Language (Middleton et al., 2015; Yeomans et al., 2019). Others can operate as plug-ins to existing GIS software such as the GeoTrace toolbox for QGIS (Thiele et al., 2017).

Many of these semi-automated methods achieve their results through very different approaches, be it through targeting edges, or minima in the data, or through different methods such as pixel-based compared to object-based. Regardless, the key to a successful semi-automated algorithm is effective feature extraction to best enhance desirable structures and minimise the inclusion of spurious lineaments. Various feature extraction methods exist, and it is beyond the scope of this study to discuss them all, however, the application of the tilt derivative to LiDAR data (Middleton et al., 2015) and to bathymetry data (Yeomans et al., *in review*) has proven highly effective. A comparison of the tilt derivative to more classical enhancement techniques, such as the Gradient, Sobel and Laplacian filters as well as the hillshade transform, found that the tilt derivative was more successful at creating continuous lineaments that were consistently sensed across and entire region of interest (Yeomans et al., *in review*).

Despite the focus on semi-automated methods, manual analyses are not without merit. Smaller manual studies, over representative subsets of a much larger study area, can help validate semi-automated lineament sets. Alternatively, it may be necessary to fill in data gaps using another dataset that may not be available for the whole area or be impractical as input to a semi-automated algorithm. However, it should be noted that subjective bias is easily introduced and, over large areas, becomes time-consuming and lacks reproducibility (Masoud and Koike, 2006; Scheiber et al., 2015).

To date, lineament detection studies, semi-automated or manual, have largely focused on augmenting their results by incorporating multi-sourced datasets. The approach has found success where lineaments that may have different signatures can be detected across different datasets and be incorporated into a final analysis. Some semi-automated methods do this within a single analysis (e.g. Masoud and Koike 2011, 2017; Yeomans et al., 2019). Some studies have looked at different resolution datasets (e.g. Meixner et al., 2017) but not within a single analysis. Combining different resolution data to map larger areas in greater detail is presently the frontier of lineament detection methods.

Data and Methods

Three lineament sets are generated within this study area. A semi-automated approach using an adaptation of the bottom-up OBIA method by Yeomans et al. (2019) is conducted to detect lineaments across the whole region of interest and a workflow is presented in Figure 3A. Methods for data processing and lineament detection are presented as well as a detailed account post-processing that is required. A smaller manually digitised lineament set is generated to validate the semi-automated analysis. Both of these lineament sets are generated from a combination of onshore LiDAR and offshore bathymetric data. A third set is generated to fill in the data gap between the onshore and offshore datasets using aerial photography.

INSERT FIGURE 3 (workflow + masks)

Data

The LiDAR data were collected as part of the collaborative Tellus South West project, and the LiDAR survey was conducted by the British Antarctic Survey between the July - August 2013. The LiDAR dataset has a spatial resolution of 1 point per meter and the data are accurate to 10 cm (both horizontal and vertical accuracy) Gerard (2014). The Digital Terrain Model (DTM) was downloaded from the Centre of Ecology and Hydrology repository in ascii grid format at 1 m pixel resolution. The onshore part of the study area covers approximately 227 km^2.

Bathymetric data were downloaded from the Admiralty Data Portal under an Open Government Licence and included five blocks of multi-beam bathymetric data collected between 2008 and 2016. These were downloaded in raster format at 2 m pixel resolution. The multi-beam bathymetry data in the study area revealed an expansive area of submerged bedrock offshore. The data extend from the nearshore environment some 10 km from the shoreline and have an approximate coverage of 423 km^2.

Proximal to onshore areas, a roughly NE-SW trending area of sediment covered seafloor is present resulting in no bedrock for lineament mapping. More localised patches of seafloor cover are present in other areas but are often small and not detrimental to the overall dataset. In rare, but spectacular cases, sand waves have formed on the seafloor and have the potential to cause artefacts in the data. These potentially problematic areas are included in subsequent analysis and dealt with in the post-processing.

The immediate nearshore areas can lack data coverage, likely due to tides, poor sea conditions during acquisition or treacherous waters making acquisition too dangerous. This can lead to a gap when combined with the onshore LiDAR and result in the phenomenon referred to as the 'white ribbon' (Mason et al., 2008). To mitigate missing data in the onshore-offshore elevation model, optical aerial photography of the coastal zone and immediate nearshore was downloaded from the EDINA Digimap repository under an educational licence. The initial data were supplied in 3-band raster format at 25 cm pixel resolution. This dataset was used to supplement lineament mapping in the area and attempt to bridge data gaps where they exist.

Object-based Image Analysis

The use of Object-Based Image Analysis (OBIA) tools have been increasingly applied in recent years. The approach makes use of raster input datasets to identify groups of pixels that are defined as “image objects” through a process of image segmentation. The approach can use a variety of segmentation methods including top-down (thresholding) and bottom-up (merging) to identify image objects (Diamant, 2004; Dragut et al., 2010; Eisank et al., 2014). These image objects are linked through a topology that describes their spatial relationship to one another and allows the calculation of geometric properties and internal statistics based on the subset pixels. The approach provides a profusion of metrics to compare, merge and/or classify image objects.

OBIA has been increasingly used in lineament detection studies such as Mavrantza and Argialas (2006), Rutzinger et al. (2007) and Marpu et al. (2008) but most recently through the workflows developed by Middleton et al. (2015) and Yeomans et al. (2019). A key step in these studies is the use of the tilt derivative transform for initial feature extraction prior to applying an OBIA workflow. An initial top-down OBIA method by Middleton et al. (2015) made use of airborne magnetic and LiDAR data separately to generate lineament networks. This approach was developed by Yeomans et al. (2019) to integrate multiple datasets (airborne magnetic, LiDAR and radiometric data) into a single workflow and produce a composite lineament network. A complementary bottom-up method was also produced, which sacrificed some detail in metadata and lineament length but was computationally more efficient is considered more desirable for larger datasets (Yeomans et al., 2019). Other feature extraction methods have been tested on bathymetric data by Yeomans et al. (*in review*), exploring the use of gradient and Laplacian filters and the hillshade transform in comparison to the tilt derivative, but were found to underperform where steep gradients (e.g. palaeocoastlines) in the seafloor were present in the data. It is assumed that this extends to subaerial steep gradients such as present-day coastlines.

Data processing

The five bathymetric data blocks were initially converted from Bathymetric Attribute Grid (.bag) files to a Geotiff format and merged into a single dataset. A visual inspection revealed that, despite the use of near-shore CCO data, some missing data were still present in the final product producing a so-called “white ribbon” between onshore and offshore areas (Mason et al., 2008). Further, it was noted that the join between nearshore Channel Coastal Observatory (CCO) data and UKHO bathymetric data had a minor step. This is likely due to the higher resolution acquisition of the CCO data and minor differences between the Admiralty Chart Datum and Ordnance Datum to which these datasets are reduced for UKHO and CCO, respectively. The step was noted and revisited during post-processing.

The merged data were resampled to 5 m pixels prior to clipping to the study area and forms the first input layer to the semi-automated lineament detection. To generate the two other input layers the LiDAR data were integrated with the bathymetric data to combine a single elevation model which was subsequently resampled to 10 m and 20 m pixel resolution.

Once the three layers were prepared, the data were exported to ascii format and imported into the Oasis Montaj 9.7 package where the data were processed using the tilt derivative transform within the MAGMAP GX package. The tilt derivative, commonly applied to potential field data such as gravity and magnetic datasets, can be applied to non-potential field data by calculating the vertical derivative by convolution as illustrated in Equation 1.

$$TDR = \tan^{-1}\left(\frac{\frac{\partial T}{\partial z}}{\sqrt{\left(\frac{\partial T}{\partial x}\right)^2 + \left(\frac{\partial T}{\partial y}\right)^2}}\right) \qquad (1)$$

where *T* is the target pixel; *x*, *y* are horizontal derivatives; and *z* is the vertical derivative.

The tilt derivative is a useful tool for lineament detection methods because it normalises the magnitude of features preserving minor lineaments in the presence of larger features (Miller and Singh, 1994; Verduzco et al., 2004; Fairhead et al., 2006). It also produces more continuous features where the feature may show minor variations along strike (Verduzco et al., 2004) and normalises the data using the arctangent where the zero contour passes over or near the edge of a feature (Miller and Singh, 1994).

Lineament detection

The lineament detection workflow applied in this study develops the bottom-up methodology first outlined by Yeomans et al. (2019). The workflow is outlined in Figure 3 which adapts the line extraction steps to include different resolution datasets that are tuned to extract lineaments based on the observable geomorphological features. The workflow is conducted in the eCognition software package using the Cognitive Network Language.

Firstly, lineaments are extracted using a rectangular kernel comprised of three stripes oriented in the long axis of the kernel. The kernel can be rotated and iterated through 360° and for this study an interval of 5° was selected. A lineament is identified using the central stripe of pixels and is given a weight based on the similarity on either side of the central stripe using the border two stripes. The majority of lineaments in the study area are assumed to be represented by minima in the data where the they have been preferentially eroded. The output of the line extraction is “lineness” raster for each input dataset which are subsequently merged (giving equal weight) into a single raster.

Following line extraction, bottom-up image segmentation is employed using the *multi-resolution* segmentation tool. The image is divided into many, differently sized image objects which are subsequently merged based on their spectral, statistical, textural, geometric or topological properties. The process also incorporates cleaning steps that remove spurious image objects based on their area, and length-width ratio to ensure that the length of lineaments is maximised. Furthermore, this analysis allows the designation of major and minor lineaments in the metadata. The threshold for this is user defined and is based on the relative similarity of features (as defined by the kernel during lineament extraction) rather than a geological measure of importance.

The final step in the lineament detection processes is to convert image objects to vector format. Given the polygonal nature of an image object, these are simplified to vector lines to produce a skeleton of the image object and a main line (principal axis) of the image object. The two forms allow the main lineament to be identified by also preserve branches should significant lineaments be conjoined. Given that only NW-SE features have been targeted in this instance, the main line vector file was taken forward.

Post-processing

The output vector lines have been post-processed to include segment length and orientation. These were calculated based on the polyline geometry within a GIS where the orientation of polylines was calculated in the range 0-179°. Furthermore, a spatial join was used to create two fields, one for between bedrock type and another for location in the onshore or offshore environment. These were appended to the attributed table for the data.

Due to the semi-automated nature of the lineament detection algorithm, due diligence was conducted to ensure lineament quality for both onshore and offshore lineaments. Upon visual inspection it was apparent that areas of sediment cover and sand waves in the bathymetric data had generated artefacts during the transformation using the tilt derivative. Therefore, post-hoc removal of potential spurious lineaments was conducted using the approach developed by Yeomans et al. (*in review*) that implements the Terrain Ruggedness Index (TRI) to map areas of sediment cover. The TRI is used to identify smooth areas which are assumed to represent sediment cover where the submerged outcrop on the seafloor is rough. These areas can be preferentially selected by using a threshold. In this study, the 5 m resolution offshore data were used to calculate the TRI layer which was normalised to 0-1 and a threshold of 0.0025 was selected using a heuristic approach. This threshold was used to generate a mask (Figure 3B) that selected all lineaments wholly within the mask and removed them.

Sediment cover in the bathymetric data cannot be fully addressed through a TRI mask. Due to the presence of sand waves in some areas causing a ripple effect on the surface, the "smoothness" criteria was not a panacea. Therefore, a manual mask was created that identified 11 areas of sand waves and these were removed where lineaments fell wholly within the mask. Additionally, a step in the bathymetry data was noticed around the southern extent of the study area, likely pertaining to a significant time gap between acquisitions. The lineaments generated immediately over the join between the two bathymetric datasets were manually removed by directly editing the shapefile.

Further post-processing of the onshore areas was conducted to remove field boundaries and roads. In Cornwall, these can be particularly problematic to semi-automated lineament detection due to the presence of "Cornish hedges", tall granite walls covered with earth, which result in a similar feature to desirable lineaments. It is possible that hedges and field boundaries removed in this step follow subtle geological features and result in a loss of data, however, due to their problematic response and small scale, the accurate mapping of these features is unlikely to be reliable. In this case, it was noticed that most of these spurious lineaments are generated from the 10 m resolution layer whereas the 20 m resolution layer had few errors. On this basis, the 20 m resolution layer was smoother where target values in the tilt derivative would be smeared out and less susceptible to the misidentification. As a consequence, to identify these artefacts and remove them, post-processing began by selecting all onshore lineaments and filtering to reduce the population based on lineaments with a length < 300 m and with a TDR value > -0.5 in the 20 m resolution layer (i.e. lineaments with TDR values (t) in the range -0.5 > t >= 1.57 that are < 300 m in length were removed). As an additional step, all lineaments with a length < 50 m in onshore areas were also removed.

The extensive post-processing steps described here demonstrate the importance of due diligence when processing large datasets from multiple sources. Careful examination of the lineament set over the region of interest identified likely spurious features caused by a variety of artefacts, each of which required a different approach to remove and ensure quality. Of the original 28350 lineaments derived from the OBIA algorithm, a total of 10009 were removed leaving a final lineament population of 18341 to be taken forward for analysis; a full breakdown is given in Table 1.

INSERT TABLE 1 (removed lineaments)

Manual mapping

Manual lineament mapping has been conducted twice in this study to complement the semi-automated methods. We selected a 7 x 7 km area that demonstrates the detail within the offshore data that is beyond the scope of being captured by our semi-automated method. We also manually digitised lineaments that were present at a local scale within the white ribbon using aerial photography. This lineament set attempts to bridge the data gap between onshore LiDAR and offshore bathymetry and provide insight into lineament populations at even higher resolution.

Offshore environment

The sub-area of interest is a 7 km^2 region straddling the west coast of the Land's End peninsula between Botallack in the southwest and Morvah in the northeast. The fault network was mapped from high-resolution multi-beam bathymetry of the offshore region and airborne LiDAR data into the onshore portion of the area at a pixel resolution of 2 m. The majority of the submerged bedrock is inferred to be Mylor Slate Formation with the exception of bedrock immediately offshore of the Land’s End Granite coastal exposure (BGS Geology, 2000; Goode and Taylor, 1988).

The multi-beam bathymetry and LiDAR data were imported into a GIS for interpretation where a hillshade transformation was applied to accentuate fault traces. It is common practice to generate two orthogonal hillshades and map lineaments in both illuminations to minimise bias (Scheiber et al., 2015). For this study, illumination source azimuths of 315° and 225° with an altitude of 45° were used for the transformation. Analysis of the structures within this sub-area was conducted manually, by hand-digitising lineaments at a consistent scale 1:5000. The scale was chosen as a reflection of Tobler's rule where a minimum map scale is determined by multiplying the pixel resolution by 2000. The 1:5000 scale was therefore chosen as close to this minimum map scale but also to reflect common mapping scales.

Nearshore environment

The nearshore environment is often a problematic area when linking between onshore and offshore datasets. The process of merging a digital elevation model with a bathymetric dataset often results in a gap in the data; the so-called white ribbon (Mason et al., 2008). The missing data in this area can vary depending on the data source and a workflow by Leon et al. (2013) attempted to create a seamless elevation model over areas that have multiple spatial and temporally separate elevation datasets. Other studies have used field observations and geological mapping to supplement the data gap (Sanderson et al., 2017; Westhead et al., 2018). Neither have been permissible to-date as a continuous study around the west Cornwall peninsula, therefore in this study, we turn to the use of aerial photography to map the nearshore, wave-cut platform and immediately onshore areas.

In this study area, the white ribbon is not pervasive around the whole coastline. It is largely constrained to the west and north coasts which have more inclement weather and have the least protection in periods of high swell compared to the south coast. Mapping of the nearshore environment was conducted around the entire coast in the study area. Aerial photography at 25 cm pixel resolution, available from EDINA Digimap resources on an Education and Research licence, was downloaded and a 250 m buffer around the coast was used to extract and mosaic the relevant image tiles. Lineaments were then manually digitised at a fixed scale of 1:500. Manual mapping was necessary due to the complexity of the image with highly varied outcrop shapes including steep slopes and wave-cut platform; the changing environment between shallow water and vegetated areas affecting the image texture; and the difficulty of removing the effects of shadows.

Results and Discussion

Herein, the three different lineament sets generated in this study are presented individually and their respective populations are discussed. The results are compared and contrasted based on their respective method of collection (semi-automated or manual mapping). These lineament sets are then further explored based on underlying bedrock to make inferences about the structural geology of the region and the implications for geothermal energy exploitation.

Semi-automated multi-scale lineament extraction

The results of the semi-automated lineament detection study are presented in Figure 4. The study detected lineaments at a regional scale from a range of resolutions covering both onshore and offshore areas and provides a composite set of lineaments derived from several datasets from a single analysis. The use of three input datasets processed at different resolutions (5 m, 10 m and 20 m pixels) allows the capture of a range of lineaments that may display different characteristics. This is particularly effective for identifying fault traces that have a different geomorphologic expression in onshore areas, which may be heavily incised, compared to offshore areas. Additionally, it allows the capture of more detailed lineament networks observable in the seafloor which are masked onshore by soil cover.

INSERT FIGURE 4 (semi-automated lineaments)

The semi-automated lineament network generated for the whole study area pictured in Figure 4A clearly demonstrates the difference in detail between onshore and offshore areas. At this scale, the onshore areas are dominated by large valley features and these can exhibit long lineament lengths and appear to be dominated by a NW-SE orientation. Conversely, the lineaments mapped in the offshore bathymetry display significantly more detail, which is illustrated in Figure 4C,D. The nature of exposure for these features likely reflects the different erosion regimes. Onshore areas are dominated by terrestrial drainage compared to offshore areas where the exposed bedrock was likely formerly a subaerial platform (Healy, 1996; Waller and Long, 2003) that has been submerged and stripped of vegetation and superficial sediment and may have subsequently been modified by wave-dominated processes in the marine environment.

The rose diagram for the lineaments (Figure 4B) has been created using the guidelines laid out by Sanderson and Peacock (2020) and uses an equal-area wedge. The equal-area diagram is superior to the conventional equal-radius approach because it better demonstrates more subtle preferred orientations. For comparison, equal-radius rose diagrams are included within the Supplementary Information and illustrate the overemphasised principal orientations.

For the lineaments detected through semi-automated methods, there is an E-ESE trend that dominates the population followed by a second more diffuse NW-N grouping and minor NE-trending contribution. Inspection of the data suggest that the ESE-WNW group represent either bedding-parallel faults or recessive features related to the erodibility of different sedimentary packages. The E-ESE orientation contrasts with the dominant ENE-E trend of bedding within the Devonian sedimentary successions to the east of the Land's End Granite (Leveridge, 2011; Leveridge and Shail, 2011). Therefore, the area is considered to highlight an anomalous scenario of potentially important lineaments in the region.

In Figure 4C, large structures trending NNW-SSE are observable with subordinate NE-SW structures and ubiquitous ENE-WSW to ESE-WNW components. The area is underlain by Devonian slates of the Gramscatho Group and demonstrates that the NW-SE trends from the onshore areas are continued offshore but manifest with a clockwise rotation towards the NNW. Additionally, the ESE-WNW trending lineament set as well as subordinate occurrences of E-W and NE-SW features are mostly present in offshore bathymetry and are poorly defined in the onshore LiDAR data. Furthermore, it is possible that these orientations of lineaments may exist in onshore areas and need to be considered in future reservoir characterisation studies for geothermal resources.

Figure 4D provides an example where the NW-SE lineaments observed onshore are clearly evident in offshore areas, too. This area is underlain by Permian granite and supports the theory that NW-SE structures are related to the granite similar to the onshore lineaments. It is worth noting that in this area, however, the spacing of these NW-SE lineaments is much closer in the offshore bathymetry than detected in the onshore LiDAR data. This may indicate that there are higher fracture densities present at a spacing of approximately 200 m, compared to the apparent kilometre spacing of NW-SE valley systems from onshore area.

Manual lineament mapping and analysis

Manual lineament mapping was conducted over a small subset of the study area to assist in validating the semi-automated methods but also to highlight the detail available in the bathymetric data offshore that exists. The results are displayed in Figure 5.

INSERT FIGURE 5 (offshore manual lineaments)

The subset is only a small representation of study area (Figure 5A) but demonstrates the complex fault network with an array of orientations (Figure 5B) that is attempted to be detected through the semi-automated methods (Figure 5C). There is a predominant orientation of NNW-trending lineaments but NE-trending features are also prominent (Figure 5D). The relationship between these systems is difficult to unpick from lineament analysis alone but both main sets appear to mutually cross-cut each other suggesting multiple reactivation episodes, as highlighted in Figure 5E.

The rose diagram for the data, shown in Figure 5B, demonstrates that lineaments predominately trend NW-NNW with a subordinate NNE-NE group present and also a clear sub-population of E-W trending lineaments. These are clearly discernible in the map where the NW-NNW and NNE-NE groupings are related to the fault network. The E-W grouping, as discussed in the semi-automated analysis, is likely either bedding-parallel faulting or the detection of recessive areas in the sedimentary succession but is perhaps under-represented compared to the semi-automated method. The manual and semi-automated interpretations are discussed in more detail below.

Detecting lineaments in the "white ribbon"

Lineaments derived from manual mapping in the nearshore environment are presented in Figure 6. These lineaments, captured around the entire coastline are mapped at a higher resolution (1:500) compared to the manual validation study (1:5000) and semi-automated method (1:10000 to 1:20000). These lineaments help to bridge the gap in the white ribbon between the onshore LiDAR data and the offshore bathymetry and provide a better understanding of the local scale structure.

INSERT FIGURE 6 (coastal manual lineaments)

The equal-area rose diagram in Figure 6B shows a dominant trend of NNW-oriented lineaments but shows that all other orientations have some degree of representation in the lineament set implying a much more complicated lineament network at this scale. The main trend is surprisingly well-defined in its NNW orientation which is far clearer compared to the semi-automated and manual validation study. The population also appears to pick up ENE and NNE trending groups that have a slightly higher abundance than other orientations. Both of these sets are not as well represented at larger scales, both in this study and from regional analysis (e.g. Yeomans et al., 2019).

Figure 6A shows four localities chosen to demonstrate the small-scale lineaments identified within the white ribbon between the two datasets. Figure 6C shows Gurnard's Head and the prevalence of lineaments that can be detected here from aerial photography. The digitised lineaments in this area do not appear to reflect the orientations of those detected in the semi-automated lineament set. This may indicate that at more local scales, the lineament network is more complicated.

Figure 6D shows the Pendeen Cliffs to the west of Portheras Cove where regular sets of NW-SE tending lineaments which reflect those detected in the semi-automated set. The manual analysis also contains NNW and NE-ENE orientations that intersperse the NW sets but are not apparent in offshore or onshore areas within the semi-automated method.

Figure 6E is located over Kenidjack Cliffs, between Botallack and Cape Cornwall, where the manual lineaments populate the white ribbon in the data and show a complex mix of WNW-ESE, NE-SW and N-S features. This area demonstrates a broad agreement with the general trends observed in the semi-automated lineament set.

Figure 6F highlights that major NW-SE lineaments extend from onshore into offshore areas. Between these features, few lineaments are detected in the bathymetry or LiDAR, but manual coastal interpretations show that a complex network exists between large scale features, reflecting the complexity highlighted in Figure 6C. The apparent increase in complexity between these major NW-SE faults, derived from the high-resolution manual mapping, is another factor to consider in future reservoir characterisation studies.

Comparing manual and semi-automated lineaments

The three lineament sets presented in this study provide a useful comparison not only for quantifying the effectiveness of the multi-scale semi-automated method, but also for identifying sampling bias at different scales.

The population statistics for the number of lineaments and their lengths for each set are presented in Table 2. The semi-automated lineament set has vastly higher numbers of lineaments compared to the two manual studies, therefore, area normalised counts are also included. When comparing the semi-automated and offshore manual sets, the semi-automated approach samples just over twice the number of lineaments detected by the manual analysis. Conversely, the lineament set mapped in the white ribbon has a vastly higher area-normalised count. This is likely due to the much finer pixel resolution (0.25 m) and the fixed scale of 1:500 during manual digitisation despite a small study area.

INSERT TABLE 2 (lineament stats)

The statistics regarding lineament length show marked variation between the sets. The longest lineament lengths are achieved in the offshore manual lineament set where mean lengths are approximately three times the length of those in semi-automated lineament set. This is also reflected in the median and standard deviations for the two sets indicating that it is reasonably robust to suggest that the semi-automated method underestimates lineament lengths by a factor of three, or, in practical terms, only sense one third of the true lineament length. This is not surprising given the semi-automated nature and the along-strike variability of many features. Manual analyses allow the human eye to link across subtle changes in the lineament profile or texture, whereas a semi-automated method relies on the continuity of the target features.

The semi-automated approach, where pixels are clustered into image objects, is for all intents and purposes an unsupervised machine learning approach. Therefore, it follows that on such a large dataset the accuracy of true lineaments must be balanced against the natural variation in the features being detected and the principals of the bias-variance trade-off from data science transcend the analysis (Friedman,1997). Maximising the continuity of lineaments often comes with a cost and, in this case, the bias would relate to how closely the target feature is mapped. A high bias identifies the target feature more closely and results in shorter (but statistically accurate) lineament segments. To mitigate this, the bias can be reduced allowing more freedom, however, the variance will increase resulting in more spurious lineaments being detected.

With respect to the white ribbon manual lineament set, the approach appears to sense very short lineaments. However, width of the area of study must be considered where this was limited to a buffer zone 250 m either side of the coastline. This causes an inherent windowing of the data along a coastline that is weathered and eroded based on local geological features, commonly faults. To this end, the manual analyses should be interpreted with a level of caution. Therefore, comparison of lineament lengths for this set with others is perhaps fallible, although the orientation data is still valid.

For comparison, the orientation data for each lineament set has been reproduced in Figure 7. It should be noted that the count data for the lineament sets in Table 2 are testament to the requirement for using equal-area rose diagrams for comparison between the lineament sets due to the significantly different population sizes (Sanderson and Peacock, 2020). When examining the two manual sets (Figure 7B,C), a clear NW-NNW grouping can be seen. The main modal trend for the manual offshore set is approximately 325° compared to the white ribbon set that is aligned 340°. A broad NW-SE grouping can be seen in the semi-automated lineament set (Figure 7A), however, the dominant orientation is ESE-WNW group with a modal trend of 095°. This may be due to the manual analyses having not detected as many ESE-WNW because of unconscious bias towards major NW-SE features where ESE-WNW trends may be more subtle or not considered to represent a fault. It could also be a question of scale as any subordinate population for ESE-WNW lineaments in the white ribbon set are subsumed into a broader general population.

INSERT FIGURE 7 (main rose diagrams)

Bedrock controls on lineament orientation

Lineaments in all three sets show multimodal populations, some more subtle than others. These modal groupings may be explained by different bedrock types and reflect the protracted structural evolution of the area. The rocks within the study area comprise granite from the Land's End pluton and the sedimentary succession of the Devonian Gramscatho Group made up of a sequence of metamorphosed mudstone-greywackes interspersed with mafic sheets. For simplicity, the region has been divided into a “granite” and “mudstone” subdivisions as these are the dominant rock types.

Lineament orientations

In Figure 8, equal-area rose diagrams are presented that depict the granite and mudstone subdivisions for the semi-automated lineament set. There is a significant change in modal trends between granite and mudstone subdivisions. The granite subdivision (Figure 8A) displays a strong NW-SE trend that is not in the mudstone subdivision (Figure 8B) exhibiting a more diffuse grouping exists across the NW-SE quadrants. Both subdivisions express a strong lineament grouping that trends approximately ESE-WNW. These observations are explored further through the different environments within which we sense these lineaments.

INSERT FIGURE 8 (rose diagrams granite-mudstone)

Figure 9 highlights the differences between lineaments detected in an onshore versus offshore environment. Figure 9A,B present lineaments detected over onshore area for both the granite and mudstone subdivisions, respectively. It can be seen here that granite lineaments have an intense modal population of NW-SE trending features with a more subdued ESE-WNW trend. In comparison, the mudstones show a dominant ESE-WNW trend but, perhaps surprisingly, mimic the NW-SE trend observed in the granite subdivision. The mudstones also demonstrate other orientations of lineaments such as NNW-SSE and NE-SW features that are less prevalent in the onshore granite set. When compared with offshore areas in Figure 9C,D, the lineaments in the offshore granite subdivision have a noticeably subdued NW-SE trend and are dominated by ESE-WNW trending features. Again, the ESE-WNW group is observed in the offshore mudstone subdivision and the broad grouping in the NW-SE quadrants that was noted in Figure 9B is also apparent but with a stronger skew towards a NNW-SSE trend.

INSERT FIGURE 9 (rose diagrams granite-mudstone by onshore-offshore)

Geological implications

Results in Figure 9 give new insight into the structural evolution of the area and highlight how different environments may influence the lineament analysis. Across both mudstone and granite subdivisions, there is a consistent ESE-WNW grouping of features. It is likely that in the mudstone subdivision this is the result of either lineaments being detected along Variscan (late Devonian-Carboniferous) bedding-parallel faulting or the detection of recessive features in the Devonian sedimentary succession due to the interbedding of mudstone and sandstone horizons. However, the same reasoning cannot be applied to explain the similar feature set observed in the granite due to its non-sedimentary nature, and the much younger Permian age. Therefore, this lineament grouping is considered to be caused by bedding-parallel faulting in the adjacent Devonian mudstones. These have subsequently been reactivated during Permian (D3) extension, thus causing faulting of the Permian granite. This interpretation agrees with the model of Shail & Alexander (1997) where extension resulting in reactivation of earlier Variscan thrusts caused zones of distributed shear, detachments and high-angle faults. The only aspect of this theory that is difficult to reconcile is that the ESE-WNW trend observed in this study is at odds with the ENE-WSW observations further east by Shail & Alexander (1997) and the prior works of Alexander & Shail (1995, 1996). It is beyond the scope of this study to investigate further but this discrepancy may be due to a number of factors such as: smaller scale structures being observable in the field; a sampling bias in either the field due to available outcrop or from the semi-automated lineament detection; or due to the slightly different locality where data for their studies have been collected immediately to the east of this study.

The semi-automated lineament population also demonstrates that there is a general divergence between the granite and mudstone subdivision when analysing lineaments in the NW-SE quadrants. The granite subdivision shows a much more distinct NW-SE trend compared to the diffuse grouping observed in mudstone (Figure 9A-D). Additionally, the onshore mudstone subdivision shows a similarly distinct NW-SE trend that is observed in the granite subdivisions. The strong NW-SE trend in granite is likely to reflect later Permian faulting and the formation of mineralised lodes in the St Just Mining District (oriented NW-SE; Dines 1956) and related to later a "reactivation" episode according to Shail and Alexander (1997). In the case of the granite, the generation of NW-SE faults at this time likely created new features in the rock mass, whereas in the mudstone pre-existing features, such as Variscan NNW-SSE structures, are likely to have accommodated any strain resulting in reactivated fault zones. Structural inheritance influencing fault systems in this manner is not new and has been attributed to perversions in lineament orientations by a number of studies (Meixner et al., 2017; Samsu et al., 2020). The trend in onshore mudstone lineaments is considered to be a local effect of nearby granite, most likely at depth influencing the fracture pattern observed in what would be the roof zone of the covered pluton.

Remote sensing implications

It has been demonstrated in this study that lineament detection can be conducted across both marine and terrestrial environments in a single analysis. However, it is noted that the nature of onshore and offshore data can yield different subpopulations of lineaments and the implications need to be considered. The observation that the granite subdivision displays a distinct change in modal trend for NW-SE lineaments when analysing for onshore and offshore environments is certainly worth considering. In this case, it is likely that the different geomorphological features of onshore areas and the prolonged exposure to terrestrial erosion processes have preferentially weathered these major fault systems. Coupled with the landcover of onshore area, these are simply the most dominant features observable in onshore areas. Conversely, notwithstanding the fact that NW-SE features are less prevalent and most likely manifest as NNW-SSE lineaments in offshore mudstones, these similar features are not less frequent, but simply less dominant in offshore areas. By using high-resolution bathymetry that contains areas of submerged outcrop the semi-automated lineament detection method is able to map structures that are unobservable in onshore areas. Given the large areas of submerged outcrop in this study, it is clear that simply detecting lineament in onshore areas would give a considerably biased representation of lineaments in the region. Therefore, where applicable, particularly in coastal regions, it is recommended that bathymetric data should be included as part of an analysis where the data are available.

An initial investigation of geothermal flow pathways

The lineament networks detected and analysed in this study are key to understanding the deep geothermal fluid flow pathways in southwest England. These are aligned sub-parallel to the contemporary maximum horizontal stress that has an approximate NW-SE orientation (Heidbach et al., 2018). These structures can be explored further to give insight into the likely width of damage zones and their potential as fault-hosted geothermal reservoirs.

In order to investigate the width of the damage zones, the regional semi-automated lineament set was first converted to a density map of structures within the orientation (a) range $120° > a > 175°$. This map was used in conjunction with the existing lineament sets to identify and manually digitise structures with long strike-lengths where only segments have been identified in the semi-automated set. The output of this manual analysis resulted in 64 major structures being identified across the study area; illustrated in Figure 10. These were used to extract lineaments from both the semi-automated and white ribbon sets within 1000 m of each structure and subset by their distance from a structure (s): $0 < s \leq 10$ m; $10 < s \leq 50$ m; $50 < s \leq 100$ m; $100 < s \leq 200$ m; $200 < s \leq 400$ m; $400 < s \leq 1000$ m. The semi-automated set provides a consistent lineament set across the whole area whereas the white-ribbon set has the advantage off bridging the data gap between bathymetry and LiDAR and providing a higher resolution lineament set. The offshore manual lineament set was not included due to its significant overlap with the semi-automated method which would bias the analysis.

INSERT FIGURE 10 (map of digitised structures)

INSERT FIGURE 11 (equal-area rose diagrams of subset lineaments)

The orientation of derived subsets for these major NW-SE structures are presented in Figure 11. The lineaments at <= 10 m from a structure in Figure 11A show a clear NW-SE to NNW-SSE likely representing the main fault system as it rotates due to changes in bedrock from granite to mudstone. An ESE-WNW group is also prevalent suggesting that this trend, originally observed at a regional level, may be pervasive and exist within these fault systems. Subordinate ENE-WSW and NNE-SSW lineaments are apparent. The ENE-WSW set is derived specifically from the white ribbon lineament set (see Supplementary Information), which was mapped at a fixed scale of 1:500, indicating that this fault set is only observable at small scales. These sets, observable at such local scales, are an important observation and may act as potential barriers or be permissive to flow within the reservoir.

The main trends in Figure 11B,C mimic those in Figure 11A, however, the subordinate ENE-WSW trend becomes less distinct. At increasing distance from the main fault strands, Figure 11D shows a slightly diminished NW-SE to NNW-SSE trend, and particularly >200 m for Figure 11E,F, it is apparent that a global trend is being captured that reflects the rose diagram in Figure 4B. This change towards a global population of ESE-WNW dominant lineaments indicates the limit of any damage zone that may exist relating to major NW-SE faults. Based on the observations in Figure 11, it is interpreted that there is a clear zone where NW-SE lineaments dominate up to 100 m away from these main fault strands, with the potential for this to extend slightly further given the diminished trend in the 100-200 m subset.

Therefore, approximately NW-SE structures, that are potential targets for deep geothermal exploitation in southwest England, have been demonstrated to be extensive, but complicated in nature. There is an apparent deflection from NW-SE to NNW-SSE when moving from granite to mudstone. Examination of offshore granite areas suggests that NW-SE structures may be present at higher density (Figure 4D), approximately every 200 m, greatly enhancing the prospect of finding new targets. By analysing lineament subsets that step away from major NW-SE faults, damage zones can be interpreted that may be slightly greater than 100 m in width. It is tentatively suggested that these damage zones may form the primary reservoir for fluids within the fault-hosted geothermal systems being targeted. However, it has been demonstrated that at local scales, subordinate lineament populations exist within these zones.

These initial observations will form the basis for future reservoir characterisation studies and the generation of Discrete Fracture Networks for the modelling of the reservoir behaviour of NW-SE fault-controlled geothermal systems at related sites such as United Downs Deep Geothermal Power project and the Eden Geothermal project. Therefore, a more detailed understanding is required of fracture density as well as size and dip angle distributions. These will determine whether the network is close to the percolation threshold (e.g. Berkowitch 2002), which will affect the net-reservoir volume and heat extraction (e.g. Geiger & Emmanuel 2010). Also, an improved understanding of possible fracture infills, and aperture-stress relations is needed to characterise reservoir potential further (e.g. Bisdom et al., 2016; Lepillier et al., 2019). All lineaments recognised in this study correspond to fault and fracture systems that have controlled palaeogeothermal fluid flow associated with granite-related magmatic-hydrothermal mineralisation (Permian) and subsequent Triassic epithermal 'cross-course' mineralisation (e.g. Jackson et al., 1989). The latter episode is of particular interest as it reflected regional ENE-WNW extension (Shail & Alexander,1997) and, in the granites, resulted in widespread precipitation of chalcedony +/- hematite within the broad NW-SE trending fault set (Jackson et al., 1989) that is being targeted as a deep geothermal reservoir. The extent to which such infills have been re-fractured during post-Triassic faulting may exert a significant control in reservoir behaviour. While the approximately NW-SE structures currently form the main deep geothermal targets in southwest England, this study indicates that a greater number of ESE-WNW, as well as NW-SE, features may be present. Depending on their permeability characteristics and linkages with the NW-SE set, these could either aid or hinder the development of distributed flow pathways within the primary reservoir. It is also possible that the ENE-WSW to ESE-WNW fault sets, although non-optimally orientated with respect to contemporary maximum horizontal stress, could act as flow paths to more extensive secondary (non-targeted) reservoirs, outside the NW-SE fault zones.

Conclusions

In this study, a composite lineament network has been created within a single, semi-automated analysis using multi-scale input layers derived from onshore LiDAR and offshore bathymetry data. The semi-automated method adapts the bottom-up Object-Based Image Analysis approach from Yeomans et al. (2019) to allow input layers at different pixel resolution to be analysed in an efficient manner. The use of multi-scale input layers to the same lineament detection algorithm is novel and the resulting lineament network is robust. Given the 700 km^2 region of interest, lineament mapping is much more detailed than other lineament detection techniques at this scale largely thanks to the exposed bedrock in the bathymetry data. The additional detail leveraged from this dataset greatly impacts the global lineament population that is detectable when compared to onshore areas.

Despite the success of this multi-scale approach, we acknowledge that detailed post-processing is required to remove artefacts. This is not a drawback of the method, but simply a requirement for due diligence to be conducted that is complicated by the size of the study area, the combination of onshore and offshore datasets and the multiple resolutions included in the analysis. The manual analyses conducted have also complemented the semi-automated analysis demonstrating the detail available in offshore datasets whilst also filling in data gaps in the white ribbon between the main LiDAR and bathymetry datasets.

The study also set out to quantify the regional lineament network in and around the Land's End Granite, with a focus on approximately NW-SE trending structures that may be targets for fault-hosted geothermal reservoirs. These have been interpreted to be associated with different orientations, NW-SE when within granite and NNW-SSE when within mudstone. The discrepancy is attributed to the generation of new faults in the Early Permian granite and exploitation of pre-existing Variscan structures in the mudstones during a later Permian reactivation episode. The along-strike variation of some of these fault zones for geothermal energy exploration is therefore important when considering new drilling targets. Based on analyses of lineament populations from this study, these structures have been interpreted to comprise a damage zones of some 100 m wide that may act a key reservoir to fluids within these geothermal systems. Finally, the derivation of such a large and detailed lineament study is incredibly useful for providing representative input data to modelling of fracture networks and subsequent reservoir simulation.

Acknowledgements

Chris Rochelle (British Geological Survey) is thanked for comments that improved an early draft of this manuscript. CMY is funded by a NERC Highlights grant (NE/S003886/1) on the GWatt project. AH is funded by a GW4+ NERC DTP grant (NE/L002434/1). CW is funded by a NERC Highlights grant (NE/S004769/1) on the GWatt project. The authors would also like to thank Adam Matthews and Harry Scott of Cornish Lithium Ltd for their support in accessing the bathymetry data. The bathymetry data used in this study have been sourced from the UK Hydrographic Office and accessed via the Admiralty Marine Data Portal. The LiDAR data used in this study have been sourced from the Centre for Ecology and Hydrology. The British Geological Survey is thanked for making the BGS Geology 625k (DiGMapGB- 625) and BGS Geology 250k (DiGMap250k) data freely available.

Captions

Fig. 1 (**A**) Regional geology of southwest England showing the Devonian-Carboniferous sedimentary basins and Early Permian granite plutons of the Cornubian Batholith. Black box outlines area of interest for this study. (**B**) Structural model of the formation of fault systems and due to changing stress regimes through latest-Carboniferous to Late Permian (redrawn from Shail & Alexander, 1997).

Fig. 2 Simplified geology map of the study area showing the offshore extend of the Land's End Granite pluton.

Fig. 3 (**A**) Workflow used for bottom-up Object-Based Image Analysis based on Yeomans et al. (2019). (**B**) Area of masked data derived from Terrain Ruggedness Index thresholding and manual mapping of sand waves.

Fig. 4 (**A**) Regional map of the semi-automated lineament set derived from the multi-scale Object-Based Image Analysis. (**B**) Equal-area rose diagram showing the orientation of derived lineaments. (**C**) Inset over submerged outcrop in mudstone areas showing predominance of NNW-SSE features. (**D**) Inset over submerged outcrop in granite areas showing predominance of NW-SE features.

Fig. 5 (**A**) Overview showing area of manual lineament mapping in offshore areas. (**B**) Equal-area rose diagram showing the orientation of derived lineaments. (**C**) Overview of the manual lineament study over the offshore submerged platform. (**D**) Inset highlighting the structural complexity of the lineament network in this area. (**E**) Small inset demonstrating mutually cross-cutting lineaments

Fig. 6 (**A**) Overview showing area of high-resolution (1:500) manual lineament mapping in the ``white ribbon'' data gap based on aerial photography. (**B**) Equal-area rose diagram showing the orientation of derived lineaments. (**C**) Inset over Gurnard's Head showing an array of lineaments. (**D**) Inset showing NW-SE trending lineaments around the Pendeen Cliffs to the west of Portheras Cove that mimic the orientation of known mineralised lode systems. (**E**) Inset over Kenidjack Cliffs, between Botallack and Cape Cornwall, displaying a complex fault network with multiple orientations of lineaments. (**F**) Inset highlighting features around Land's End where NW-SE feature appear to extend from the onshore into the offshore between which lineaments do not share a similar orientation.

Fig. 7 Equal-area rose diagrams reproduced from Figures 4, 5 and 6 for comparison across the three lineament sets. Lineaments are derived from (**A**) semi-automated set, (**B**) manual offshore set and (**C**) white ribbon (coastal) set.

Fig. 8 Equal-area rose diagrams for subdivision of the semi-automated lineament set based on bedrock associations. (**A**) shows those lineaments that are within granite rocks with a strong NW-SE trend and subordinate ESE-WNW trend. (**B**) displays lineaments within mudstone where the ESE-WNW dominates and a broader grouping is seen in the NW-SE quadrants.

Fig. 9 Equal-area rose diagrams for subdivision of the semi-automated lineament set based on bedrock associations and their location within the onshore or offshore environment. (**A**) shows onshore lineaments in granite. (**B**) onshore lineaments in mudstone. (**C**) offshore lineaments in granite. (**D**) offshore lineaments in mudstone. Note the marked different in NW-SE oriented lineaments between onshore and offshore granite areas and the dominance and ESE-WNW trend in the latter.

Fig. 10 Overview map of manually digitised major structures with an approximate NW-SE trend. Similarly oriented structures are currently being explored further east in the southwest England for fault-hosted geothermal reservoirs. These structures have been digitised based on density of lineaments oriented 120 > *a* > 175 and the lineament sets derived in this study.

Fig. 11 Equal-area rose diagrams for subsets of lineaments (derived from semi-automated and manual "white ribbon" lineament sets) based on distance away from digitised major NW-SE structures (*s*). (**A**) 0 < *s* <= 10 m; (**B**) 10 < *s* <= 50 m; (**C**) 50 < *s* <= 100 m; (**D**) 100 < *s* <= 200 m; (**E**) 200 < *s* <= 400 m; (**F**) 400 < *s* <= 1000 m. These subsets of lineaments are used to infer the presence of damage zones, approximately 100 m in width, that may act as reservoirs to geothermal fluids.

Table 1
Breakdown of the lineaments removed during each post-processing stage, the total removed and the remaining lineaments.

Table 2
Population statistics for the count and length of lineaments across the three lineament sets where area-normalised counts have been included due to the vast difference in coverage between the three lineament sets.

References

Alexander, A. C., & Shail, R. K. (1995). Late Variscan structures on the coast between Perranporth and St. Ives, Cornwall. *Proceedings of the Ussher Society*, *8*, 398–404.

Alexander, A. C., & Shail, R. K. (1996). Late- to post-Variscan structures on the coast between Penzance and Pentewan, South Cornwall. *Proceedings of the Ussher Society*, *9*, 72–

78.

Alexander, A. C., Shail, R. K., & Leveridge, B. E. (2019). Late Paleozoic extensional reactivation of the Rheic–Rhenohercynian suture zone in SW England, the English Channel and Western Approaches. *Geological Society, London, Special Publications*, *470*, SP470.19. https://doi.org/10.1144/SP470.19

Berkowitz, B. (2002). Characterizing flow and transport in fractured geological media: A review. *Advances in Water Resources*, *25*, 861–884. https://doi.org/10.1016/S0309-1708(02)00042-8

BGS Geology. (2000). *DiGRock250k digital map*. British Geological Survey.

Bisdom, K., Bertotti, G., & Nick, H. M. (2016). The impact of different aperture distribution models and critical stress criteria on equivalent permeability in fractured rocks. *Journal of Geophysical Research: Solid Earth*, *121*, 4045–4063. https://doi.org/10.1002/2015JB012657

Chen, Y., Clark, A. H., Farrar, E., Wasteneys, H. A. H. P., Hodgson, M. J., & Bromley, A. V. (1993). Diachronous and independent histories of plutonism and mineralization in the Cornubian Batholith, southwest England. *Journal of the Geological Society, London*, *150*, 1183–1191.

Chesley, J. T., Halliday, A. N., Snee, L. W., Mezger, K., Shepherd, T. J., & Scrivener, R. C. (1993). Thermochronology of the Cornubian batholith in southwest England: Implications for pluton emplacement and protracted hydrothermal mineralization. *Geochimica et Cosmochimica Acta*, *57*, 1817–1835. https://doi.org/10.1016/0016-7037(93)90115-D

Diamant, E. (2004). Top-down unsupervised image segmentation (it sounds like an oxymoron, but it actually isn't). *Proceedings of the 3rd Pattern Recognition in Remote Sensing Workshop (PRRS'04), August 2004, Kingston University, UK*.

Dines, H. G. (1956). *The Metalliferous mining region of south-west England*. Economic Memoirs of the Geological Survey of Great Britain.

Dragut, L., Tiede, D., & Levick, S. R. (2010). ESP: A tool to estimate scale parameter for multiresolution image segmentation of remotely sensed data. *International Journal of Geographical Information Science*, *24*, 859–871. https://doi.org/10.1080/13658810903174803

Eisank, C., Smith, M., & Hillier, J. (2014). Assessment of multiresolution segmentation for delimiting drumlins in digital elevation models. *Geomorphology*, *214*, 452–464. https://doi.org/10.1016/j.geomorph.2014.02.028

Evans, C. D. R. (1990). *United Kingdom offshore regional report:The Geology of the Western English Channel and its Western Approaches*. HMSO, London.

Fairhead, J. D., & Williams, S. E. (2006). Evaluating Normalized Magnetic Derivatives for Structural Mapping. *Society of Exploration Geophysicists New Orleans Extended Abstract*, 845–849. New Orleans: Society of Exploration Geophysicists.

Friedman, J. H. (1997). On Bias, Variance, 0/1-Loss, and the Curse-of-Dimensionality. *Data Mining and Knowledge Discovery*, *1*, 55–77. https://doi.org/10.1023/A:1009778005914

Geiger, S., & Emmanuel, S. (2010). Non-Fourier thermal transport in fractured geological media. *Water Resources Research*, *46*, 1–13. https://doi.org/10.1029/2009wr008671

Gerard, F. (2014). *LIDAR QUALITY CONTROL REPORT Project: PM 1478* (Vol. 44).

Gleeson, S. A., Wilkinson, J. J., Shaw, H. F., & Herrington, R. J. (2000). Post-magmatic hydrothermal circulation and the origin of base metal mineralization, Cornwall, UK. *Journal of the Geological Society, London*, *157*, 589–600. https://doi.org/10.1144/jgs.157.3.589

Gleeson, S. A., Wilkinson, J. J., Stuart, F. M., & Banks, D. A. (2001). The origin and evolution of base metal mineralising brines and hydrothermal fluids, South Cornwall, UK. *Geochimica et Cosochimica Acta*, *65*, 2067–2079.

Goode, A. J. J., & Taylor, R. T. (1988). *Geology of the area around Penzance*. Memoir of the British Geological Survey, Sheet 351 and 358 (England and Wales).

Healy, M. G. (1996). Late Quaternary Coastal Change in West Cornwall, UK. In M. G. Healy (Ed.), *Late Quaternary Coastal Change in West Cornwall, UK*. Durham: Environmental Research Centre the University of Durham.

Heidbach, O., Rajabi, M., Cui, X., Fuchs, K., Müller, B., Reinecker, J., … Zoback, M. (2018). The World Stress Map database release 2016: Crustal stress pattern across scales. *Tectonophysics*, *744*, 484–498. https://doi.org/10.1016/j.tecto.2018.07.007

Holloway, S., & Chadwick, R. A. (1986). The Sticklepath-Lustleigh fault zone: Tertiary sinistral reactivation of a Variscan dextral strike-slip fault. *Journal of the Geological Society, London*, *143*, 447–452.

Jackson, N. J., Willis-Richards, J., Manning, D. A. C., & Sams, M. S. (1989). Evolution of the Cornubian ore field, Southwest England; Part II, Mineral deposits and ore-forming processes. *Economic Geology*, *84*, 1101–1133.

Karimi, B., & Karimi, H. A. (2017). An automated method for the detection of topographic patterns at tectonic boundaries. *The Ninth International Conferences on Pervasive Patterns* *and Applications*, 72–77.

Leon, J. X., Phinn, S. R., Hamylton, S., & Saunders, M. I. (2013). Filling the “white ribbon” - a multisource seamless digital elevation model for Lizard Island, northern Great Barrier Reef. *International Journal of Remote Sensing*, *34*, 6337–6354. https://doi.org/10.1080/01431161.2013.800659

Lepillier, B., Daniilidis, A., Doonechaly Gholizadeh, N., Bruna, P. O., Kummerow, J., & Bruhn, D. (2019). A fracture flow permeability and stress dependency simulation applied to multi-reservoirs, multi-production scenarios analysis. *Geothermal Energy*, *7*, 1-16. https://doi.org/10.1186/s40517-019-0141-8

Leveridge, B. E. (2011). The Looe, South Devon and Tavy basins: the Devonian rifted passive margin successions. *Proceedings of the Geologists’ Association*, *122*, 616–717. https://doi.org/10.1016/j.pgeola.2011.03.005

Leveridge, B. E., & Hartley, A. J. (2006). The Varisan Orogeny: the development and deformation of Devonian/Carboniferous basins in SW England and South Wales. In P. J. Brenchley & P. F. Rawson (Eds.), *The Geology of England and Wales* (2nd ed., pp. 225–256). The Geological Society, London.

Leveridge, B. E., & Shail, R. K. (2011). The Gramscatho Basin, south Cornwall, UK: Devonian active margin successions. *Proceedings of the Geologists’ Association*, *122*, 568–615. https://doi.org/10.1016/j.pgeola.2011.03.004

Marpu, P. R., Niemeyer, I., Nussbaum, S., & Gloaguen, R. (2008). A procedure for automatic object-based classification. In T. Blaschke, S. Lang, & G. J. Hay (Eds.), *Object-Based Image Analysis: Spatial Concepts for Knowledge-Driven Remote Sensing Applications* (pp. 169–184). https://doi.org/10.1007/978-3-540-77058-9

Mason, T., McVey, S., & Rainbow, B. (2008). Colouring the “White Ribbon”: Strategic Coastal Monitoring in the South-East of England. *Hydro International*. Retrieved from https://www.hydro-international.com/content/article/colouring-the-white-ribbon

Masoud, A. A., & Koike, K. (2011). Auto-detection and integration of tectonically significant lineaments from SRTM DEM and remotely-sensed geophysical data. *ISPRS Journal of Photogrammetry and Remote Sensing*, *66*, 818–832. https://doi.org/10.1016/j.isprsjprs.2011.08.003

Masoud, A., & Koike, K. (2006). Tectonic architecture through Landsat-7 ETM+/SRTM DEM-derived lineaments and relationship to the hydrogeologic setting in Siwa region, NW Egypt.

Journal of African Earth Sciences, *45*, 467–477. https://doi.org/10.1016/j.jafrearsci.2006.04.005

Masoud, A., & Koike, K. (2017). Applicability of computer-aided comprehensive tool (LINDA: LINeament Detection and Analysis) and shaded digital elevation model for characterizing and interpreting morphotectonic features from lineaments. *Computers & Geosciences*, *106*, 89–100.

Mavrantza, O. D., & Argialas, D. P. (2006). Object-oriented image analysis for the identification of geologic lineaments. *International Archives of Photogrammetry, Remote Sensing and Spatial Information Sciences*, *36*, 1–6.

Meixner, J., Grimmer, J. C., Becker, A., Schill, E., & Kohl, T. (2017). Comparison of different digital elevation models and satellite imagery for lineament analysis: Implications for identification and spatial arrangement of fault zones in crystalline basement rocks of the southern Black Forest (Germany). *Journal of Structural Geology*, *108*, 256–268. https://doi.org/10.1016/j.jsg.2017.11.006

Middleton, M., Schnur, T., Sorjonen-ward, P., & Hyvönen, E. (2015). Geological lineament interpretation using the Object-Based Image Analysis Approach: results of semi-automated analyses versus visual interpretation. *Geological Survey of Finland, Special Paper*, *57*, 135–154.

Miller, H. G., & Singh, V. (1994). Potential field tilt - a new concept for location of potential field sources. *Journal of Applied Geophysics*, *32*, 213–217. https://doi.org/10.1016/0926-9851(94)90022-1

Nixon, C. W., Sanderson, D. J., & Bull, J. M. (2012). Analysis of a strike-slip fault network using high resolution multibeam bathymetry, offshore NW Devon U.K. *Tectonophysics*, *541–543*, 69–80. https://doi.org/10.1016/j.tecto.2012.03.021

O’Leary, D. W., Friedman, J. D., & Pohn, H. A. (1976). Lineament, linear, lineation: Some proposed new standards for old terms. *Geological Society Of America Bulletin*, *87*, 1463–1469. https://doi.org/10.1130/0016-7606(1976)87<1463

Rahnama, M., & Gloaguen, R. (2014). TecLines: A MATLAB-Based Toolbox for Tectonic Lineament Analysis from Satellite Images and DEMs, Part 1: Line Segment Detection and Extraction. *Remote Sensing*, *6*, 5938–5958. https://doi.org/10.3390/rs6075938

Rahnama, M., & Gloaguen, R. (2014). TecLines: A MATLAB-based toolbox for tectonic lineament analysis from satellite images and DEMs, Part 2: Line Segments Linking and

Merging. *Remote Sensing*, *6*, 11468–11493. https://doi.org/10.3390/rs61111468

Rutzinger, M., Maukisch, M., & Petrini-Monteferri, F. (2007). Development of Algorithms for the Extraction of Linear Patterns (Lineaments) from Airborne Laser Scanning Data. *Proceedings of the Conference “Geomorphology for the Future”, Obergurgl, 2007*, 1–8.

Samsu, A., Cruden, A. R., Micklethwaite, S., Grose, L., & Vollgger, S. A. (2020). Scale matters: The influence of structural inheritance on fracture patterns. *Journal of Structural Geology*, *130*, 103896. https://doi.org/10.1016/j.jsg.2019.103896

Sanderson, D. J., Dix, J. K., Westhead, K. R., & Collier, J. S. (2017). Bathymetric mapping of the coastal and offshore geology and structure of the Jurassic Coast, Weymouth Bay, UK. *Journal of the Geological Society*, *174*, 498–508. https://doi.org/10.1144/jgs2016-070

Sanderson, D. J., & Peacock, D. C. P. (2020). Making rose diagrams fit-for-purpose. *Earth-Science Reviews*, *201*, 103055. https://doi.org/10.1016/j.earscirev.2019.103055

Scheiber, T., Fredin, O., Viola, G., Jarna, A., Gasser, D., & Łapińska-Viola, R. (2015). Manual extraction of bedrock lineaments from high-resolution LiDAR data: methodological bias and human perception. *Journal of the Geological Society of Sweden (GFF)*, *137*, 362–372. https://doi.org/10.1080/11035897.2015.1085434

Scrivener, R. C. (2006). Cornubian granites and mineralization of SW England. In P. J. Brenchley & P. F. Rawson (Eds.), *The Geology of England and Wales* (Second, pp. 257–268). The Geological Society, London.

Scrivener, R. C., Darbyshire, D. P. F., & Shepherd, T. J. (1994). Timing and significance of crosscourse mineralization in SW England. *Journal of the Geological Society, London*, *151*, 587–590.

Shail, R. K., & Alexander, A. C. (1997). Late Carboniferous to Triassic reactivation of Variscan basement in the western English Channel: evidence from onshore exposures in south Cornwall. *Journal of the Geological Society, London*, *154*, 163–168. https://doi.org/10.1144/gsjgs.154.1.0163

Shail, R. K., & Leveridge, B. E. (2009). The Rhenohercynian passive margin of SW England: Development, inversion and extensional reactivation. *Comptes Rendus Geoscience*, *341*, 140–155.

Šilhavý, J., Minár, J., Mentlík, P., & Sládek, J. (2016). A new artefacts resistant method for automatic lineament extraction using Multi-Hillshade Hierarchic Clustering (MHHC). *Computers & Geosciences*, *92*, 9–20.

Simons, B., Shail, R. K., & Andersen, J. C. Ø. (2016). The petrogenesis of the Early Permian Variscan granites of the Cornubian Batholith: Lower plate post-collisional peraluminous magmatism in the Rhenohercynian Zone of SW England. *Lithos*, *260*, 76–94. https://doi.org/10.1016/j.lithos.2016.05.010

Thiele, S. T., Grose, L., Samsu, A., Micklethwaite, S., Vollgger, S. A., & Cruden, A. R. (2017). Rapid, semi-automatic fracture and contact mapping for point clouds, images and geophysical data. *Solid Earth*, *8*, 1241–1253. https://doi.org/10.5194/se-8-1241-2017

Verduzco, B., Fairhead, D., Green, C. M., & MacKenzie, C. (2004). New insights into magnetic derivatives for structural mapping. *The Meter Reader*, 116–119.

Waller, M. P., & Long, A. J. (2003). Holocene coastal evolution and sea-level change on the southern coast of England: A review. *Journal of Quaternary Science*, *18*, 351–359. https://doi.org/10.1002/jqs.754

Westhead, R. K., McCarthy, D. J., Collier, J. S., & Sanderson, D. J. (2018). Spatial variability of the Purbeck–Wight Fault Zone—a long-lived tectonic element in the southern UK. *Proceedings of the Geologists' Association*, *129*, 436–451. https://doi.org/10.1016/j.pgeola.2017.08.005

Yeomans, C. M., Middleton, M., Shail, R. K., Grebby, S., & Lusty, P. A. J. (2019). Integrated Object-Based Image Analysis for semi-automated geological lineament detection in southwest England. *Computers & Geosciences*, *123*, 137-148 [Available Online November 2018]. https://doi.org/10.1016/j.cageo.2018.11.005

Yeomans, C. M., Head, M., & Lindsay, J. J. (*in review*). Application of the tilt derivative transform to bathymetric data for structural lineament mapping. *Journal of Structural Geology*. https://doi.org/10.31223/osf.io/akw65

	No data	TRI mask	Sand wave mask	Manual step
Removed lineaments	12	8046	1189	95
Total removed lineaments	10009			
Remaining lineaments	18341			

Field boundaries
667

Lineament set	Count	Area (sq km)	Area-normalised count	Mean
Semi-automated	18341	700	26.20	100.47
Offshore Manual	593	49	12.10	315.70
White Ribbon	7584	37.21	203.82	26.09

Standard deviation	Median	Range	Skewness	Kurtosis
98.88	71.93	2287.74	4.94	50.49
327.11	216.38	2575.90	3.48	15.77
19.25	20.95	234.17	2.80	14.19

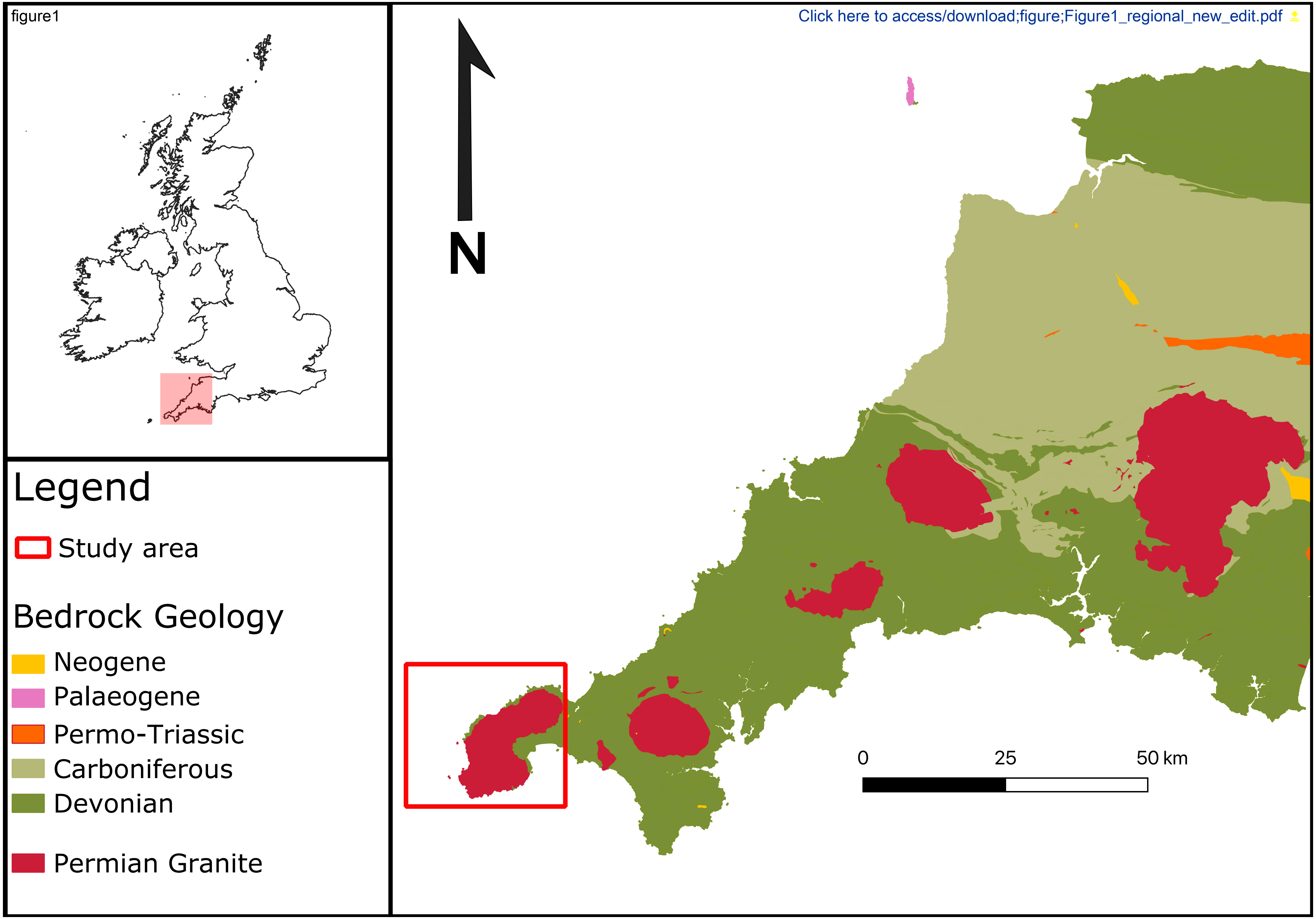
figure1
N
0
25
50 km
Legend
Study area
Bedrock Geology
Neogene
Palaeogene
Permo-Triassic
Carboniferous
Devonian
Permian Granite

figure2

Click here to access/download;figure;Figure2_local_geology_edit.pdf

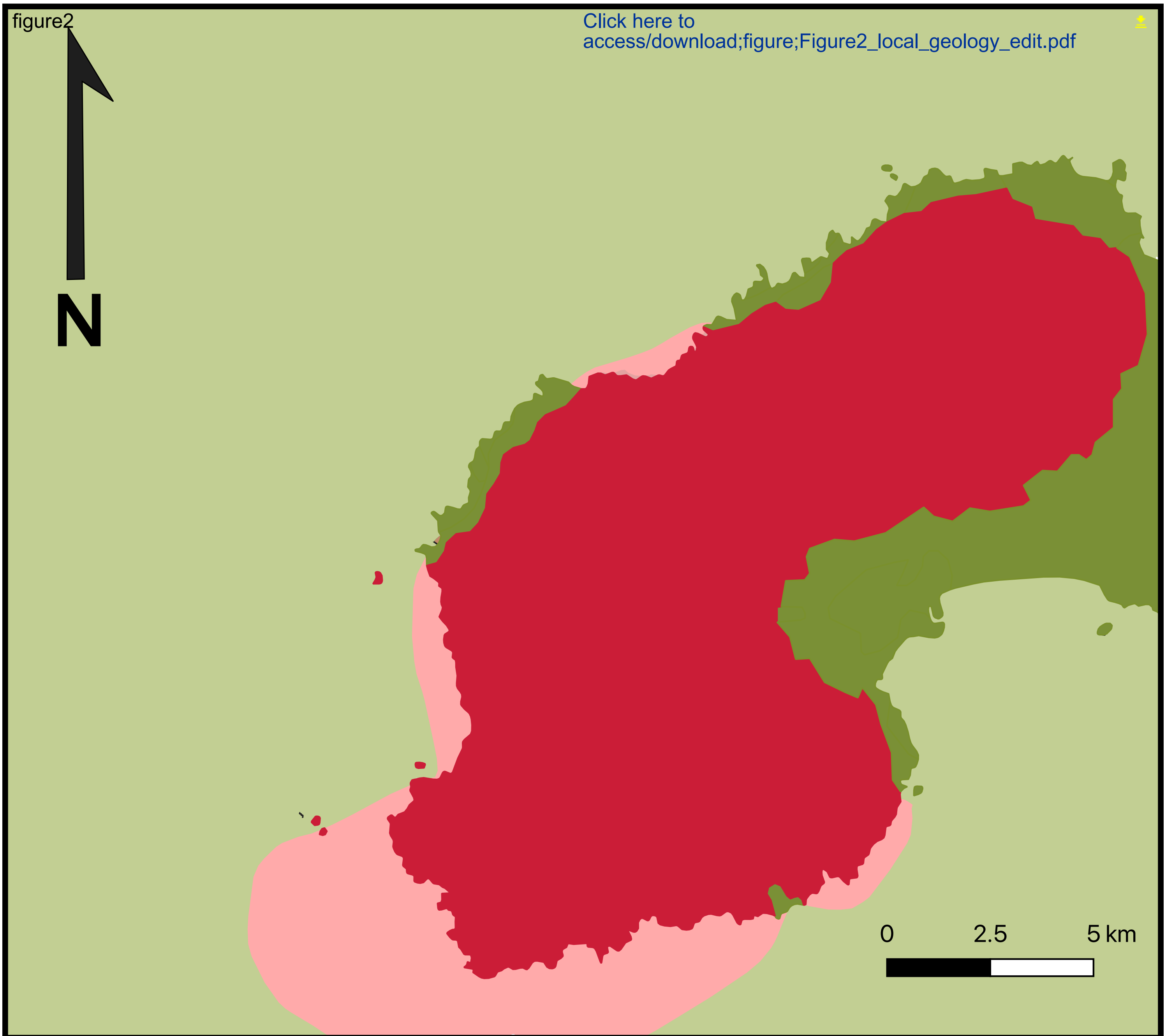

Legend

Onshore Geology

Gramscatho Group

Cornubian Granite

Offshore Geology

Gramscatho Group

Cornubian Granite

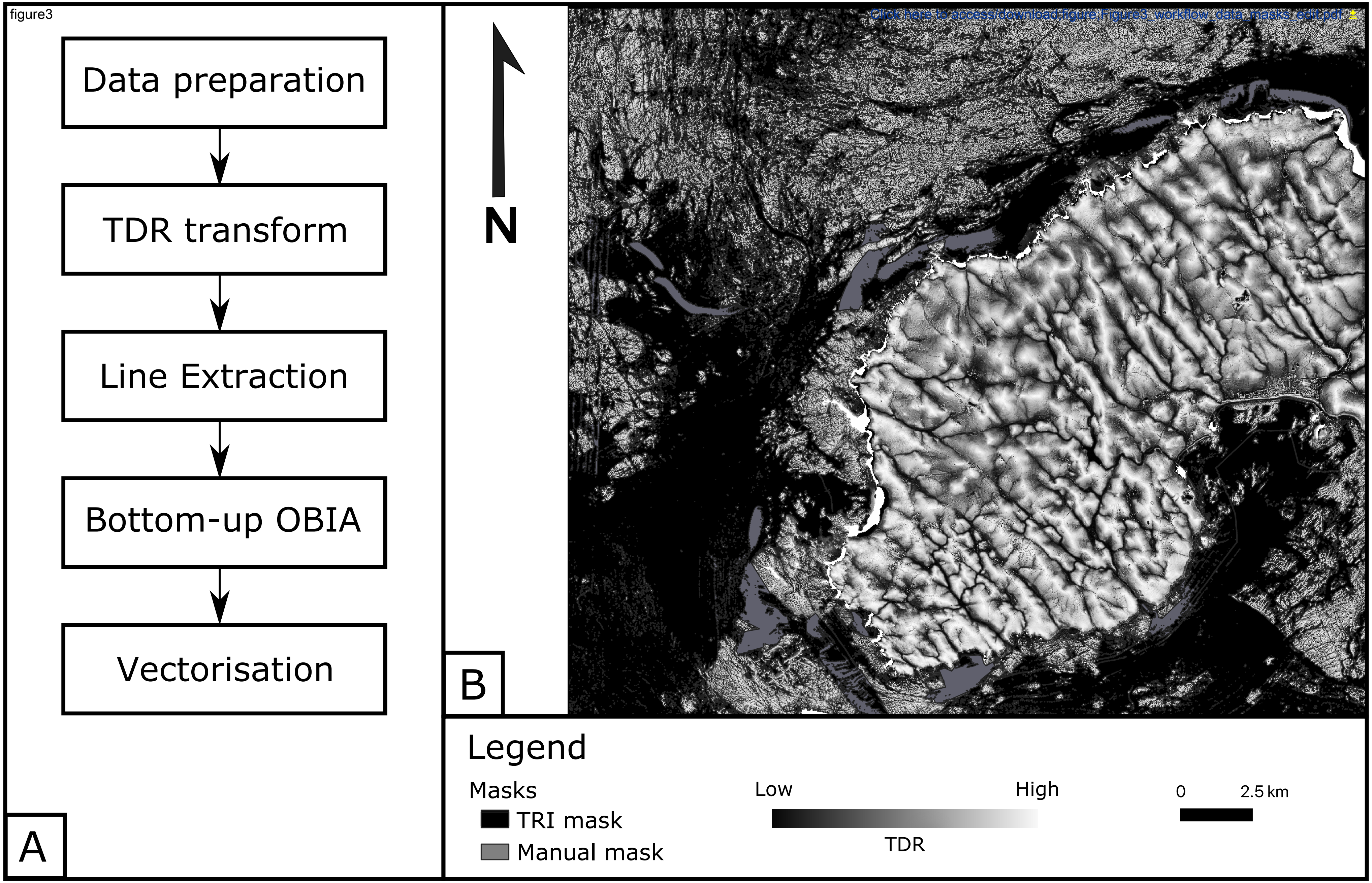
figure3
A
Data preparation
TDR transform
Line Extraction
Bottom-up OBIA
Vectorisation
B
N
Legend
Masks
TRI mask
Manual mask
Low
High
TDR
0
2.5 km

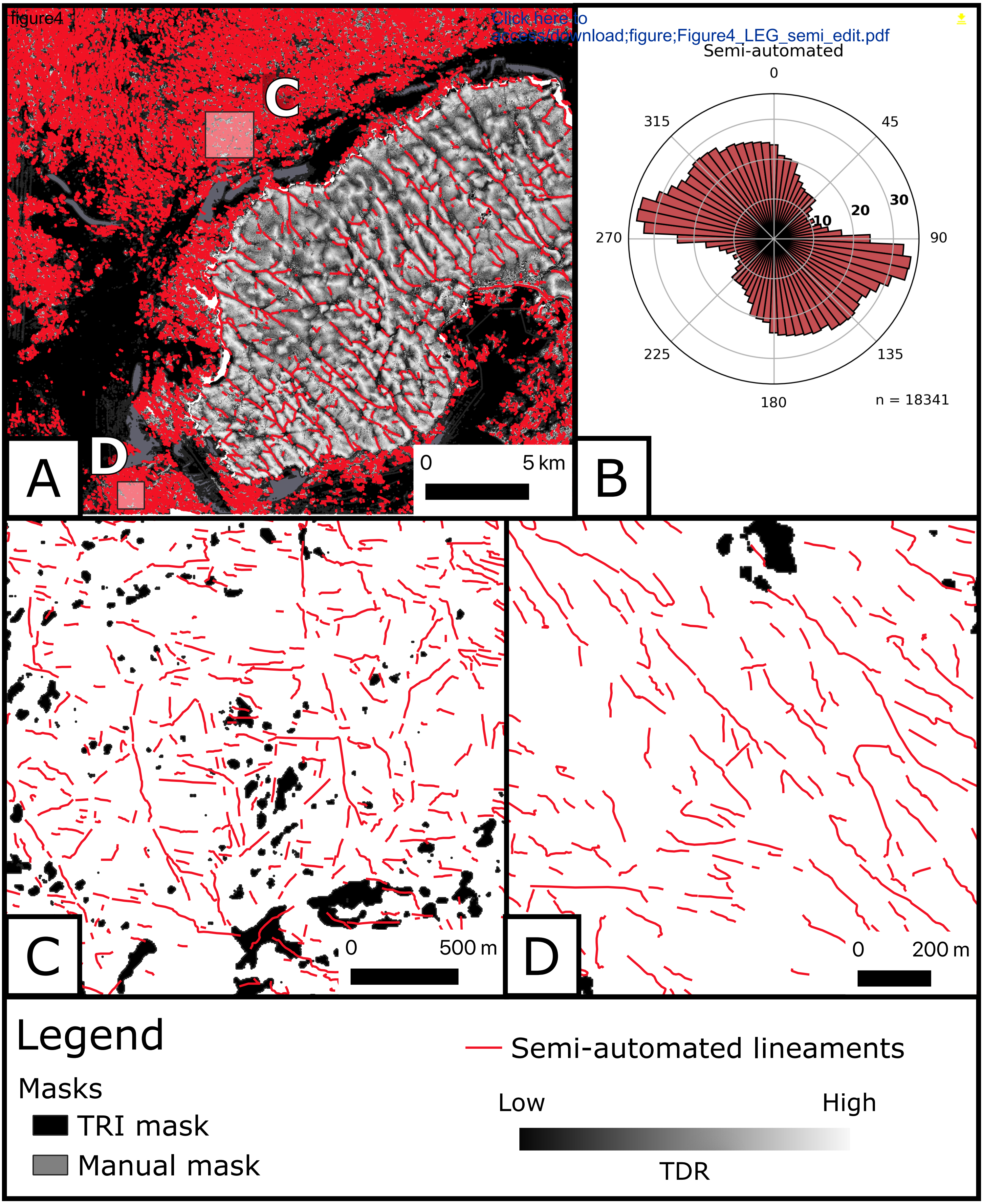
C
D
A
0
5 km
Semi-automated
0
45
90
135
180
225
270
315
10
20
30
n = 18341
B
0
500 m
C
0
200 m
D
Legend
Masks
TRI mask
Manual mask
Semi-automated lineaments
Low
High
TDR

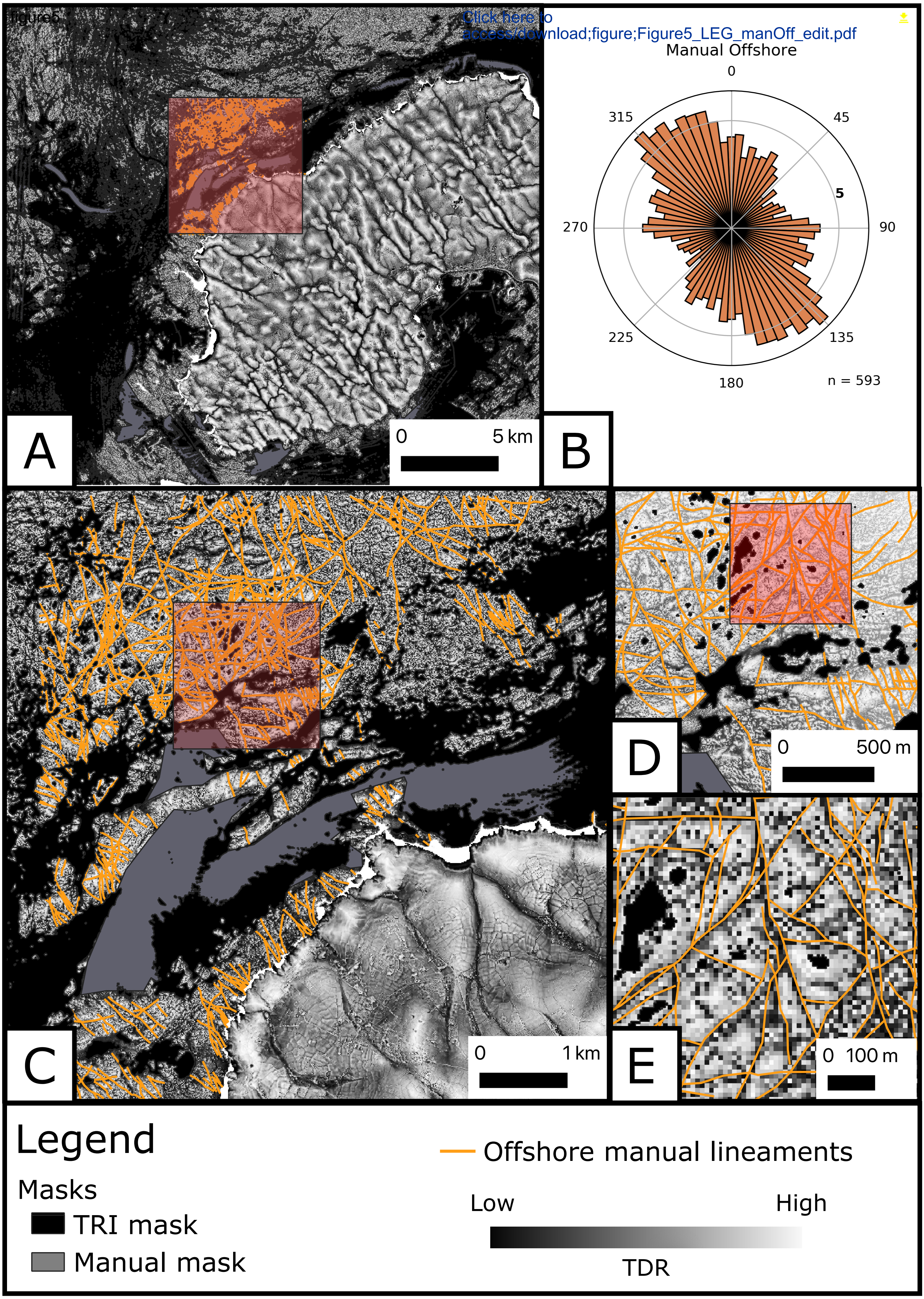
Manual Offshore
0
45
90
135
180
225
270
315
5
n = 593
A
0 5 km
B
C
0 1 km
D
0 500 m
E
0 100 m
Legend
Masks
TRI mask
Manual mask
Offshore manual lineaments
Low
High
TDR

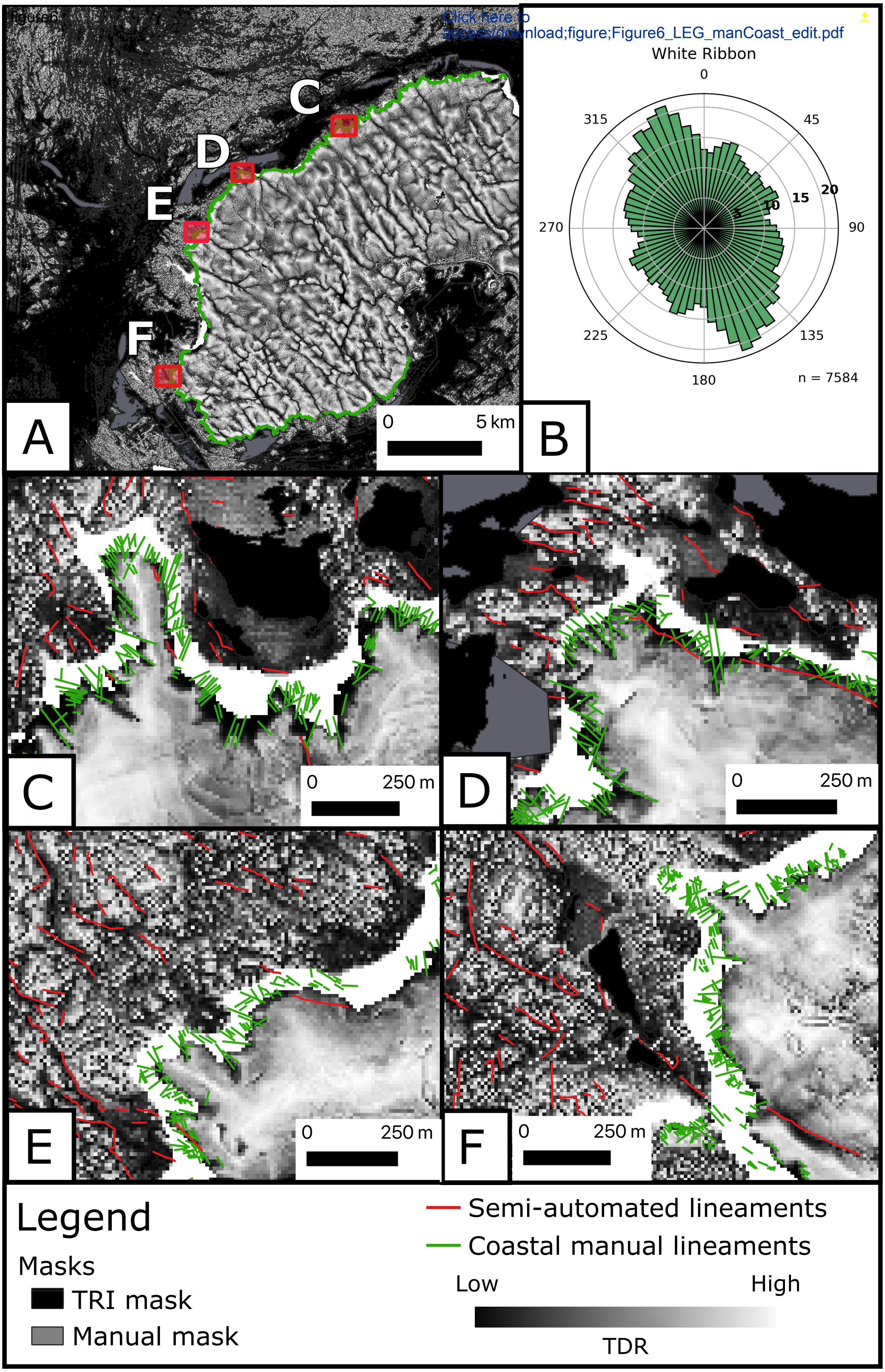
White Ribbon
0
45
90
135
180
225
270
315
10
15
20
n = 7584
A
B
C
D
E
F
0
5 km
0
250 m
Legend
Masks
TRI mask
Manual mask
Semi-automated lineaments
Coastal manual lineaments
Low
High
TDR

figure7

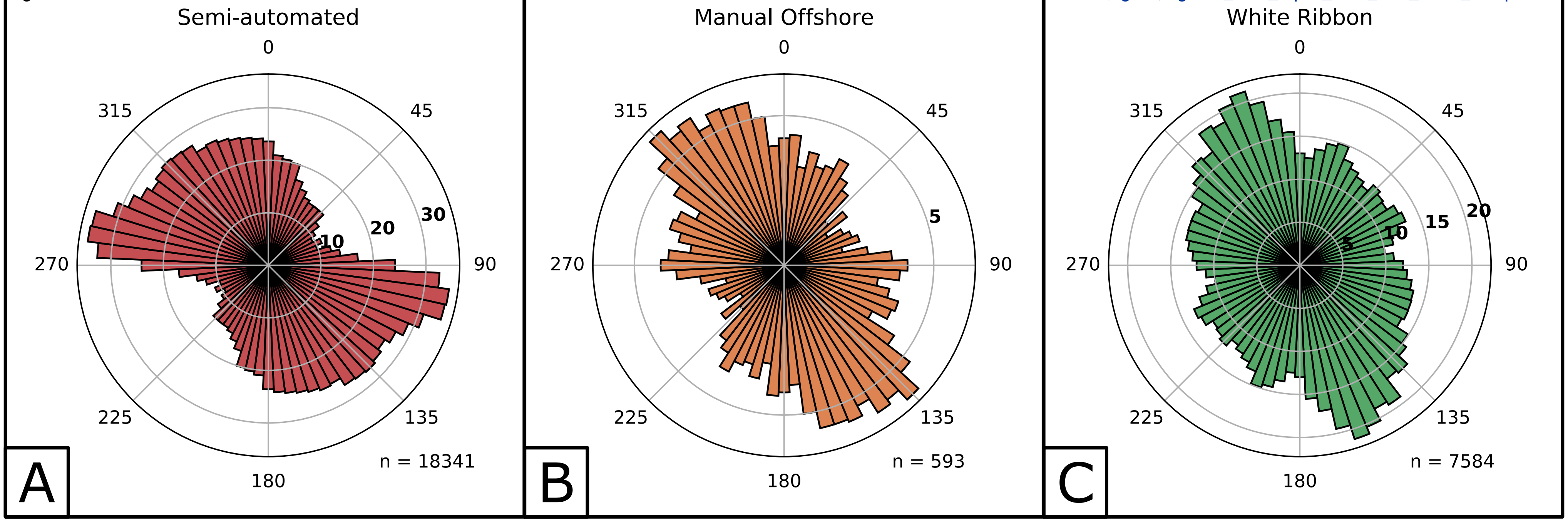
Semi-automated
0
45
90
135
180
225
270
315
10
20
30
n = 18341
A
Manual Offshore
0
45
90
135
180
225
270
315
5
n = 593
B
White Ribbon
0
45
90
135
180
225
270
315
5
10
15
20
n = 7584
C

figure8

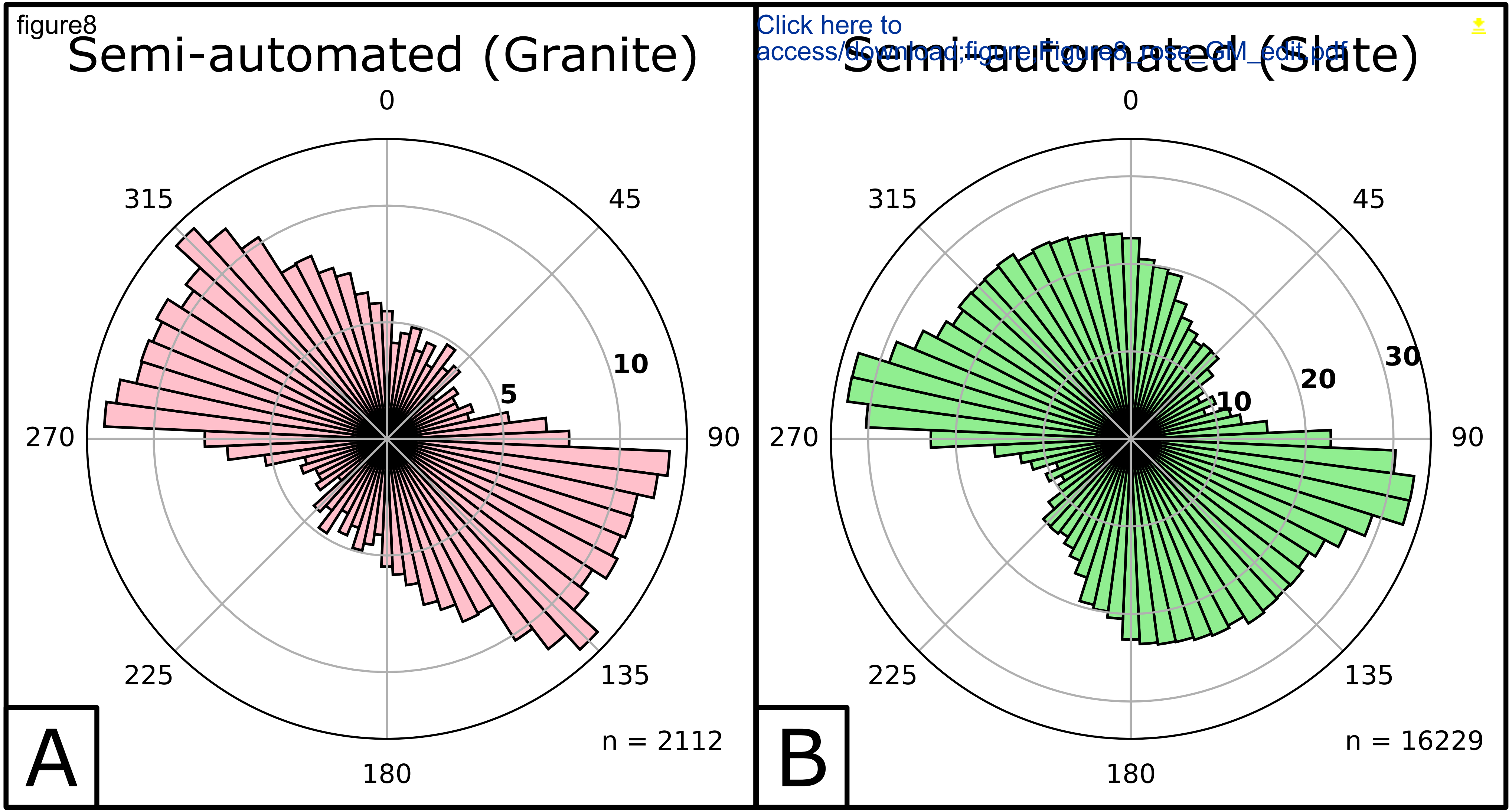
Semi-automated (Granite)
0
45
90
135
180
225
270
315
5
10
n = 2112
A
Semi-automated (Slate)
0
45
90
135
180
225
270
315
10
20
30
n = 16229
B

figure9

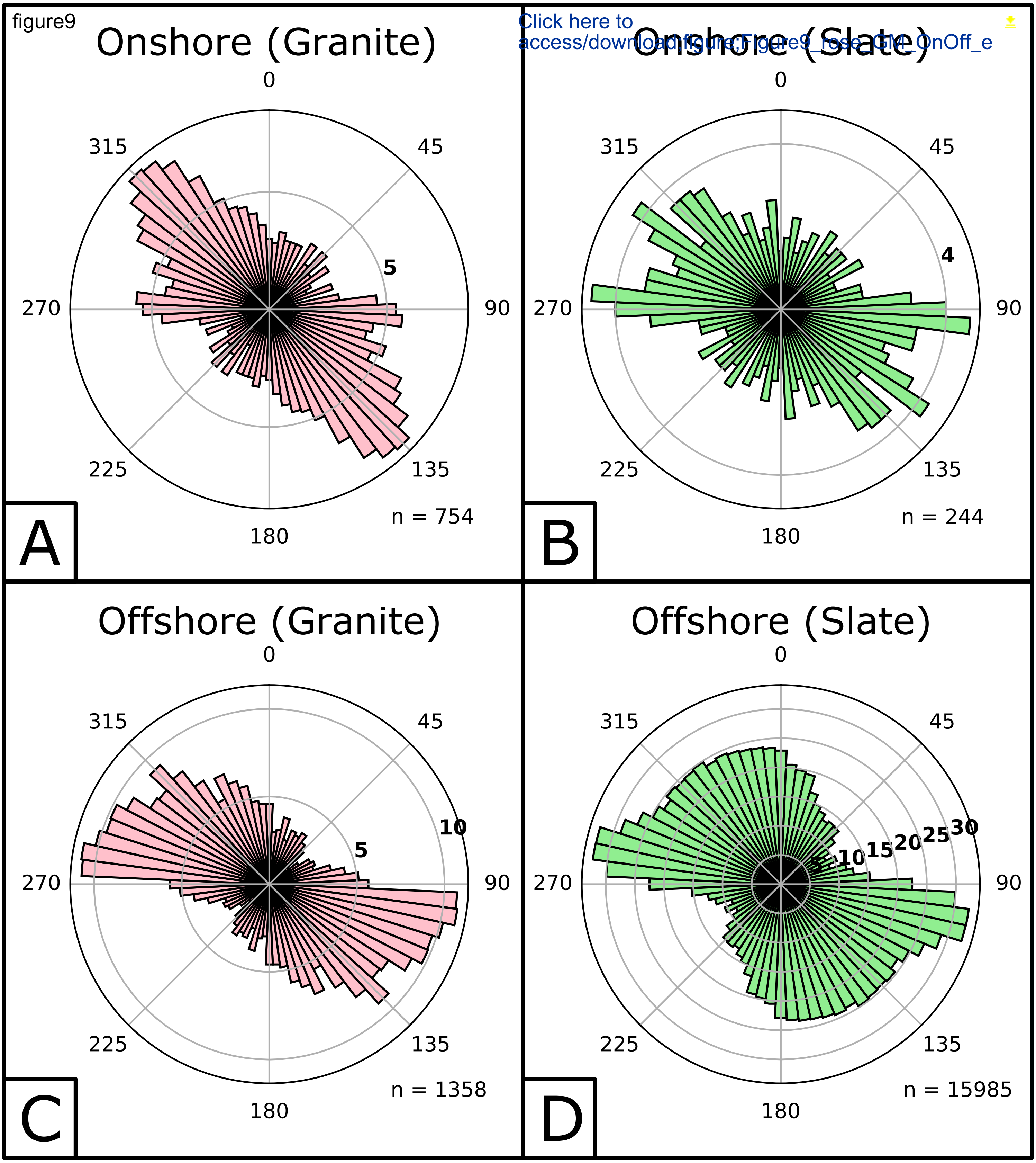
Onshore (Granite)
0
45
90
135
180
225
270
315
5
n = 754
A
Onshore (Slate)
4
n = 244
B
Offshore (Granite)
5
10
n = 1358
C
Offshore (Slate)
5
10
15
20
25
30
n = 15985
D

figure10

Click here to access/download;figure;Figure10_digitised_NWSE_edit.pdf

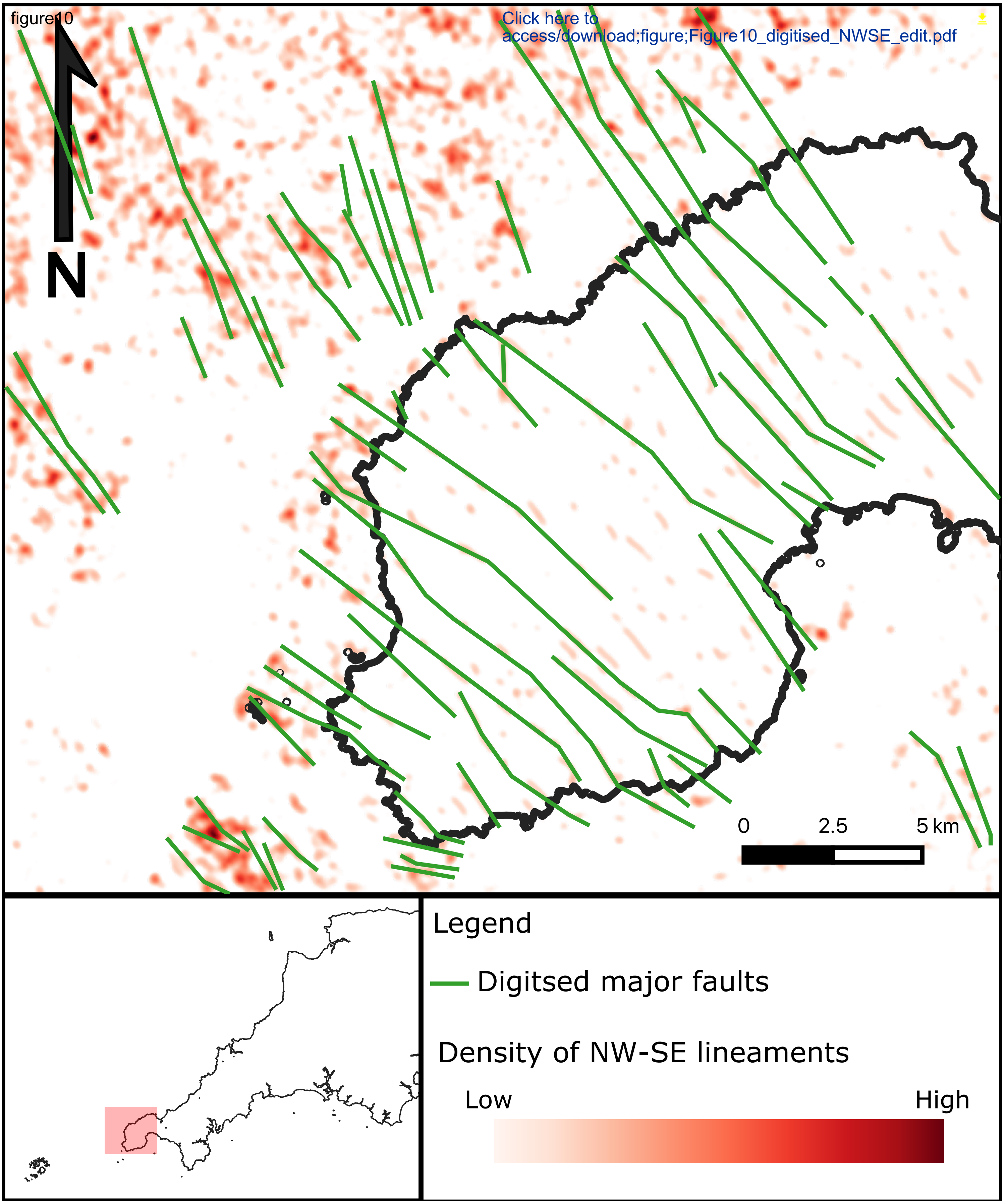

figure11

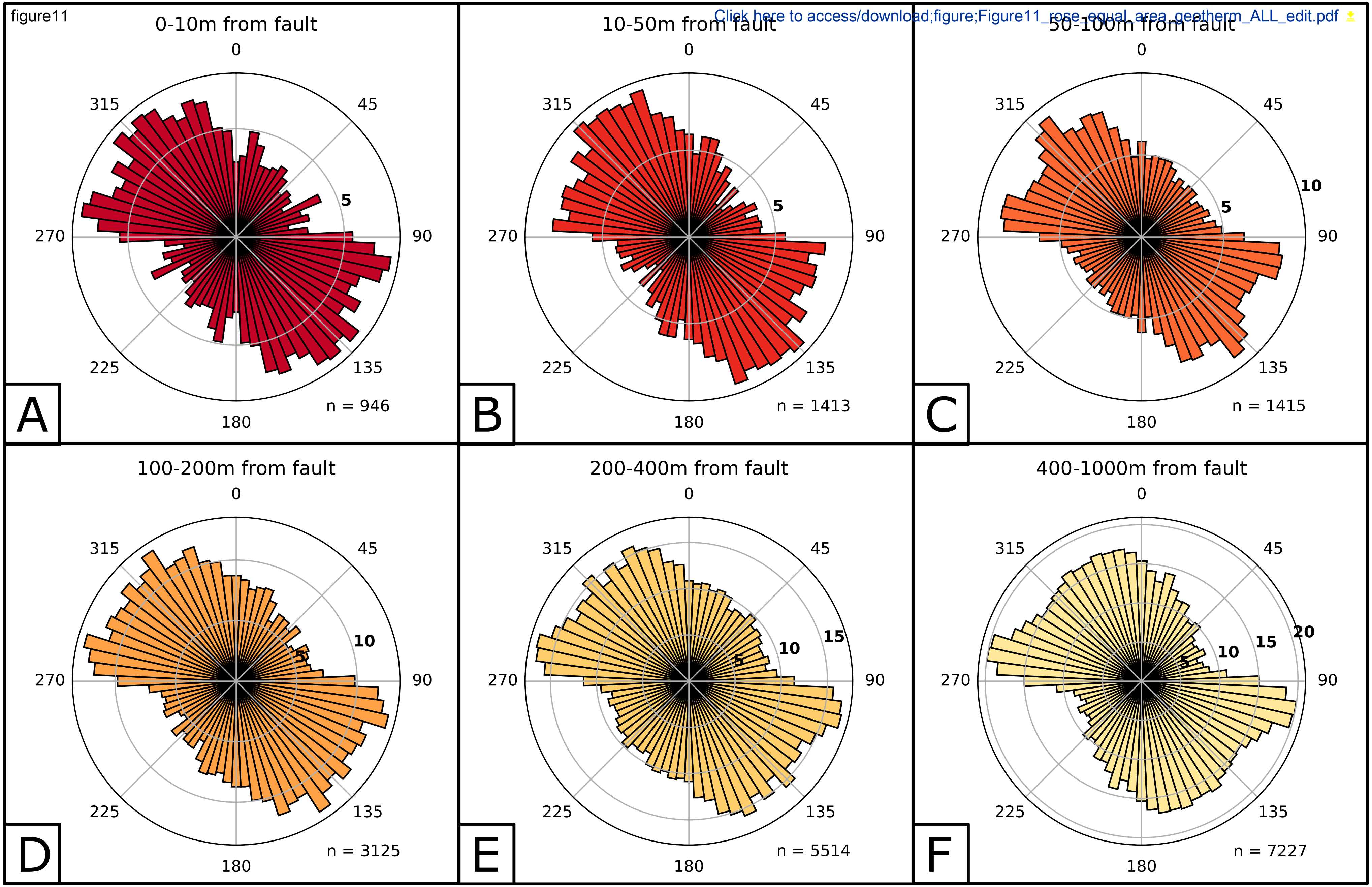

0-10m from fault
n = 946
A
10-50m from fault
n = 1413
B
50-100m from fault
n = 1415
C
100-200m from fault
n = 3125
D
200-400m from fault
n = 5514
E
400-1000m from fault
n = 7227
F
0
45
90
135
180
225
270
315
5
10
15
20